

# Classical simulability of Clifford+ T circuits with Clifford-augmented matrix product states

Zejun Liu and Bryan K. Clark

*The Anthony J. Leggett Institute for Condensed Matter Theory and IQUIST and NCSA Center for Artificial Intelligence Innovation and Department of Physics, University of Illinois at Urbana-Champaign, IL 61801, USA*

(Dated: December 24, 2024)

Generic quantum circuits typically require exponential resources for classical simulation, yet understanding the limits of classical simulability remains a fundamental question. In this work, we investigate the classical simulability of  $N$ -qubit Clifford circuits doped with  $t$  number of  $T$ -gates by converting the circuits into Clifford-augmented matrix product states (CAMPS). We develop a simple disentangling algorithm to reduce the entanglement of the MPS component in CAMPS using control-Pauli gates, which replaces the standard algorithm relying on heuristic optimization when  $t \lesssim N$ , ensuring that the entanglement of the MPS component of CAMPS does not increase for  $N$  specific  $T$ -gates. Using a simplified model, we explore in what cases these  $N$   $T$ -gates happen sufficiently early in the circuit to make classical simulatability of  $t$ -doped circuits out to  $t = N$  possible. We give evidence that in one-dimension where the  $T$ -gates are uniformly distributed over the qubits and in higher spatial dimensions where the  $T$ -gates are deep enough we generically expect polynomial or quasi-polynomial simulations when  $t \leq N$ . We further explore the representability of CAMPS in the regime of  $t > N$ , uncovering a non-trivial dependence of the MPS entanglement on the distribution of  $T$ -gates. While it is polynomially efficient to evaluate the expectation of Pauli observable or the quantum magic in CAMPS, we propose algorithms for sampling, probability and amplitude estimation of bitstrings, and evaluation of entanglement Rényi entropy from CAMPS, which, though still having exponential complexity, improve efficiency over the standard MPS simulations. This work establishes a versatile framework based on CAMPS for understanding classical simulatability of  $t$ -doped circuits and exploring the interplay between quantum entanglement and quantum magic on quantum systems.

## CONTENTS

I. Introduction	1	B. Stabilizer Tableau for Clifford Circuits	22
II. Algorithms for Converting from $t$ -doped Clifford Circuits to CAMPS	2	C. Derivation for Eq. (18)	24
A. Optimization-free Disentangling Algorithm	3	D. Improved Stabilizer Group Learning Algorithm	24
B. Improved Optimization-based Disentangling Algorithm	5	E. Alternative View on the $t$ -doped Clifford Circuits Simulation	25
C. Connection between OFD and OBD	5	F. Conjectures for an Ideal Clifford disentangling Algorithm	27
III. CAMPS for ( $t \leq N$ )-doped Clifford Circuits	8	G. Numerical Results on Pauli Obseables	28
IV. CAMPS for ( $t > N$ )-doped Clifford Circuits	11		
A. Random $t$ -doped Clifford Circuits with $L_T = 1$	11		
B. Random $t$ -doped Clifford Circuits for various $(L_T, N_T)$	12		
V. Simulation Tasks	13		
A. Probability and Sampling of Bitstring	13		
B. Wavefunction Amplitude	15		
C. Entanglement Rényi Entropy	16		
VI. Conclusions	19		
Acknowledgments	20		
References	20		
A. Concepts and Notations	22		

## I. INTRODUCTION

The power of quantum computation comes from its ability to run quantum circuits which cannot be simulated classically. Understanding this dividing line between the classes of circuits for which there exists efficient classical simulation methods and those for which the simulations are exponentially costly, either in space or time, has been a central focus in advancing our understanding of quantum systems [1–6]. Under reasonable assumptions of computational complexity, it is known that efficient classical simulation for random quantum circuits do not exist. On the other hand, classes of circuits such as Clifford circuits, matchgates, and weakly entangled circuits can be simulated in polynomial time [7–12]. Even within specific “simulatable” classical circuits, one

can separately ask about the computational difficulty in performing various tasks such as computing the observable expectation values, sampling bitstrings, calculating probabilities or amplitudes, and evaluating information-theoretic quantities like entanglement entropy.

Exploring the boundaries of classical simulability is necessary for understanding where and how we might achieve quantum advantage [6, 13–16]. It also directly affects what quantum many-body systems can be simulated and therefore understood [12, 17–22]. Given the importance in determining this classical/quantum dividing line and the paucity of circuit classes for which classical simulation currently exists, discovering new classes of quantum circuits that can be simulated in polynomial time is particularly important. In this work, we investigate the classical simulability of Clifford circuits doped with a few number of non-Clifford gates (e.g.,  $T$ -gate) for a wide range of simulation tasks.

While Clifford circuits are simulatable in polynomial time, it has been widely believed that Clifford+ $T$  circuits (see Fig. 1) have a cost which is exponential in the number of  $T$  gates  $t$  [23–26]. Recent work has developed a new representation of  $t$ -doped Clifford circuits applied to a computational basis product state as Clifford-augmented matrix-product states (CAMPS) [27, 28]. The CAMPS state is written as a Clifford circuit applied to a matrix-product state (MPS). Motivation for our work came from an observation that ‘optimally’ constructed CAMPS states saw little increase in entanglement for the first  $N$  gates (this was first mentioned in Ref. [27], and recently further discussed with respect to the representability in a series of parallel related papers [29, 30] which were posted during the final stages of our work). Because historically CAMPS states have been generated by heuristic optimization, it has been unclear regarding the origin or generalizability of this effect.

A key contribution of our result is the development of a new algorithm for generating CAMPS which makes it transparent that in many circuits there are  $N$   $T$ -gates which do not increase which do not increase the entanglement of the MPS piece from the CAMPS state and that typically these ‘free’ gates are often amongst the earliest  $T$ -gates encountered in the circuit. We model our new algorithm showing, under reasonable assumptions, what distribution of  $T$ -gates preserves these early free gates and which distributions do not. In our simplified model, we discover that  $T$ -gates distributed deeper than either  $\log(N)$  or  $\log^2(N)$  (depending on the uniformity of the distribution of gates) are typically free gates leading to polynomial or quasi-polynomial simulations for generic one-dimensional circuits of uniformly doped  $T$  gates with  $t \leq N$ . In addition, we show that the standard approach for generating CAMPS [27–31] reproduces by optimization the steps of our algorithm in most cases explaining the source of the observed behavior. In the process, we also develop modifications to the original approach of optimization which speeds it up by orders of magnitude.

Having an efficiently represented CAMPS ensures that

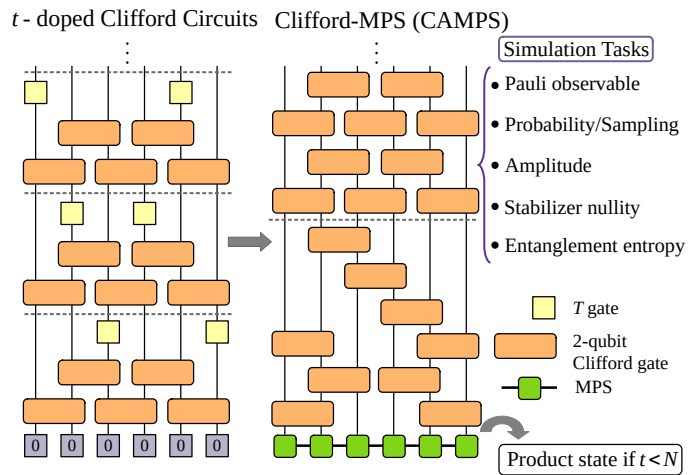


FIG. 1: (Left) Circuit architecture of  $t$ -doped Clifford circuits with  $L_T$  layers of random Clifford gates followed by  $N_T$   $T$  gates on random qubits. (Right) Transformed circuit CAMPS where  $T$ -gates have been commuted through the Clifford, absorbed into the initial state as a matrix product state and disentangled with additional Clifford gates. The MPS is nearly a product state when  $t < N$ . We consider the following simulation tasks in this work: calculation of Pauli string expectation values; sampling or determining probability of bitstrings; calculating amplitudes; determining stabilizer nullity or the stabilizer Pauli group; calculating entanglement Rényi entropy of the entire states.

expectation values of Pauli observables can be computed in polynomial time as can the stabilizer nullity, a measure for quantum magic. We explore other computational tasks including sampling, probability and amplitude estimation, and the evaluation of the entanglement Rényi entropy. While these simulation tasks still remain exponentially costly, we reveal that the CAMPS can offer improvements to various degrees over the traditional tensor-network simulation methods including the improvements in the exponent of the computational cost.

We also explore the use of CAMPS for ( $t > N$ )-doped Clifford circuits. There we find that even for evaluating Pauli observables such simulations become exponentially expensive with an exponential cost that now depends more on the structure of the circuit. In these cases the exponent can still be reduced with respect to a typical tensor-network simulation.

## II. ALGORITHMS FOR CONVERTING FROM $t$ -DOPED CLIFFORD CIRCUITS TO CAMPS

To classically simulate  $t$ -doped Clifford circuits, we can convert it to a CAMPS state where a Clifford circuit is applied to an MPS. During intermediate steps of this process, one ends up with an MPS state which can be decom-

posed as a disentangling Clifford circuit times a lower-bond dimensions MPS; we describe in this section two approaches to finding this disentangling Clifford. The previously existing approach, which we call the optimization-based disentangling algorithm (OBD), finds the disentangling Clifford using heuristic optimizations [27–31]; in Sec. II B we give an improved version of OBD with significantly reduced computational complexity. The second approach, the optimization-free disentangling algorithm (OFD), is a new constructive optimization-free technique for finding the disentangling Clifford circuit when  $t \lesssim N$ .

Either approach can be used in the typical process of representing the quantum circuit as a CAMPS. The CAMPS  $|\Psi\rangle = U_C|\psi\rangle$  is initialized with  $U_C$  as the identity operator on  $N$  qubits, and  $|\psi\rangle$  as the initial product state of the circuit. During simulation, if a Clifford gate  $C$  is encountered, to represent the new state  $|\Psi'\rangle = C|\Psi\rangle$ , we directly absorb  $C$  into  $U_C$  (see Appendix B for the method to concatenate two Clifford circuits):

$$U_C \leftarrow CU_C \quad (1)$$

If a  $T$ -gate is encountered, for example on the  $k$ -th qubit, i.e.,  $|\Psi'\rangle = T_k|\Psi\rangle = T_kU_C|\psi\rangle$ , we first commute the  $T$ -gate through the Clifford circuit  $U_C$  to obtain the corresponding twisted Pauli strings (see Appendix B for details on commuting Pauli strings). A  $T$ -gate can be written as  $T = e^{i\pi/8}(\alpha I + \beta Z)$  where  $\alpha = \cos(\pi/8)$  and  $\beta = -i \sin(\pi/8)$ ; we can disregard the global phase factor  $e^{i\pi/8}$  in subsequent steps. Then,

$$T_kU_C = U_C\tilde{T}_k = U_C(\alpha I + \beta\tilde{Z}_k) \quad (2)$$

where  $\tilde{Z}_k = U_C^\dagger Z_k U_C$  is the twisted Pauli string from  $Z_k$ . Generally, the action of  $(\alpha I + \beta P)$  on  $|\psi\rangle$ , where  $P$  is a Pauli string, introduces entanglement into  $|\psi\rangle$ . To counteract this, OFD or OBF is applied to selectively reduce part of the entanglement. The key idea is to find a Clifford circuit  $U_{\mathcal{D}}$  such that  $U_{\mathcal{D}}\tilde{T}_k|\psi\rangle$  has lower entanglement than  $\tilde{T}_k|\psi\rangle$ . This yields:

$$|\Psi'\rangle = (U_C U_{\mathcal{D}}^\dagger) (U_{\mathcal{D}} \tilde{T}_k |\psi\rangle) \quad (3)$$

and we update the CAMPS as follows:

$$U_C \leftarrow U_C U_{\mathcal{D}}^\dagger, \quad |\psi\rangle \leftarrow U_{\mathcal{D}} \tilde{T}_k |\psi\rangle \quad (4)$$

### A. Optimization-free Disentangling Algorithm

In this section, we introduce a simple Clifford disentangling algorithm – optimization-free disentangling algorithm (OFD) – aimed at disentangling  $|\psi\rangle$  using Clifford gates during the simulation. In contrast to the previously existing Clifford disentangling algorithm, which relies on heuristic optimization over the full two-qubit Clifford group [27–31], this approach constructively selects appropriate control-Pauli gates to transform the

entangled states induced by  $T$ -gates back into product states, eliminating the need for optimization. Importantly, this disentangling algorithm also sheds light on the underlying mechanism that enables classical simulability for  $(t \leq N)$ -doped Clifford circuits with CAMPS, and clarifies the conditions under which MPS entanglement growth becomes inevitable (thus impeding efficient simulation).

OFD looks at the twisted Pauli strings  $\tilde{T}_k = \alpha I + \beta \tilde{Z}_k$  from Eq. (2) along with the current initial state  $|\psi\rangle$  from CAMPS, and constructs the corresponding disentangling Clifford circuit  $U_{\mathcal{D}}$  gate-by-gate. We consider the general case in which, after the application of several  $T$ -gates (until  $t \approx N$ ), the state  $|\psi\rangle$  contains some qubits in magic states and others in  $|0\rangle$  (Initially  $|\psi\rangle = |0\rangle^{\otimes N}$  contains no magic states). Our goal is that the combined operator  $U_{\mathcal{D}}\tilde{Z}_k$  applies a non-trivial Pauli-term to at most one qubit; a non-trivial Pauli term is a Pauli operator that changes the qubit state - i.e. X,Y,Z on a magic state or X,Y on a  $|0\rangle$ . If the Pauli string  $\tilde{Z}_k$  already has this property then we do not need a disentangler. Alternatively,  $\tilde{Z}_k$  might have a non-trivial Pauli term being applied to a qubit in  $|0\rangle$  state. In such a case, we can use that qubit  $v$  as the control qubit for a set of control-Pauli gates that are applied to the qubits that are being hit with non-trivial Pauli terms (see Fig. 2(a)). This disentangling unitary has the property that  $U_{\mathcal{D}}\tilde{T}_k = \alpha I + \beta X_v$  (or  $\alpha I + \beta Y_v$  if qubit  $v$  is hit by  $Y$ ) leads to qubit  $v$  becoming a magic state. This does not increase the entanglement of the state. In the case where there are multiple Pauli-terms but no non-trivial Pauli-term on a  $|0\rangle$  qubit, then the magic states will become further entangled amongst themselves, for example as  $|\overline{mm}\rangle = \alpha|mm\rangle + \beta|m_X m_Z\rangle$  in Fig. 2(b). Even in this case, it will leave the  $|0\rangle$  qubits unentangled from the rest of the system and they are available to be used as the control qubits for subsequent  $T$ -gates.

Furthermore, we argue that OFD works independent of which control qubit is selected. Consider a simple example: in simulating the first  $T$ -gate, the MPS becomes  $|\psi''\rangle = \alpha|0000\dots 0\rangle + \beta|1100\dots 0\rangle$ . Either  $CX_{1,2}$  or  $XC_{1,2}$  (see Appendix A for the notations) can disentangle the first two qubits. For the former, we have

$$\begin{aligned} C_1^a &= CX_{1,2}, \quad U_C^a = U_C(CX)_{1,2}, \\ |\psi_2^a\rangle &= \alpha|0000\dots 0\rangle + \beta|1000\dots 0\rangle. \end{aligned} \quad (5)$$

Similarly, using  $XC_{1,2}$  gives

$$\begin{aligned} C_1^b &= XC_{1,2}, \quad U_C^b = U_C(XC)_{1,2}, \\ |\psi_2^b\rangle &= \alpha|0000\dots 0\rangle + \beta|0100\dots 0\rangle. \end{aligned} \quad (6)$$

Next, we analyze the consequences from these two different choices on the subsequent simulation of  $T$ -gates. Using Eq. (2), the Pauli strings  $P^{a/b}$ , commuted from the next  $T$ -gate, i.e.,  $\tilde{T}_k = \alpha I + \beta P^{a/b}$ , are related through:

$$P^b = C^b C^{a\dagger} P^a C^a C^{b\dagger} \quad (7)$$

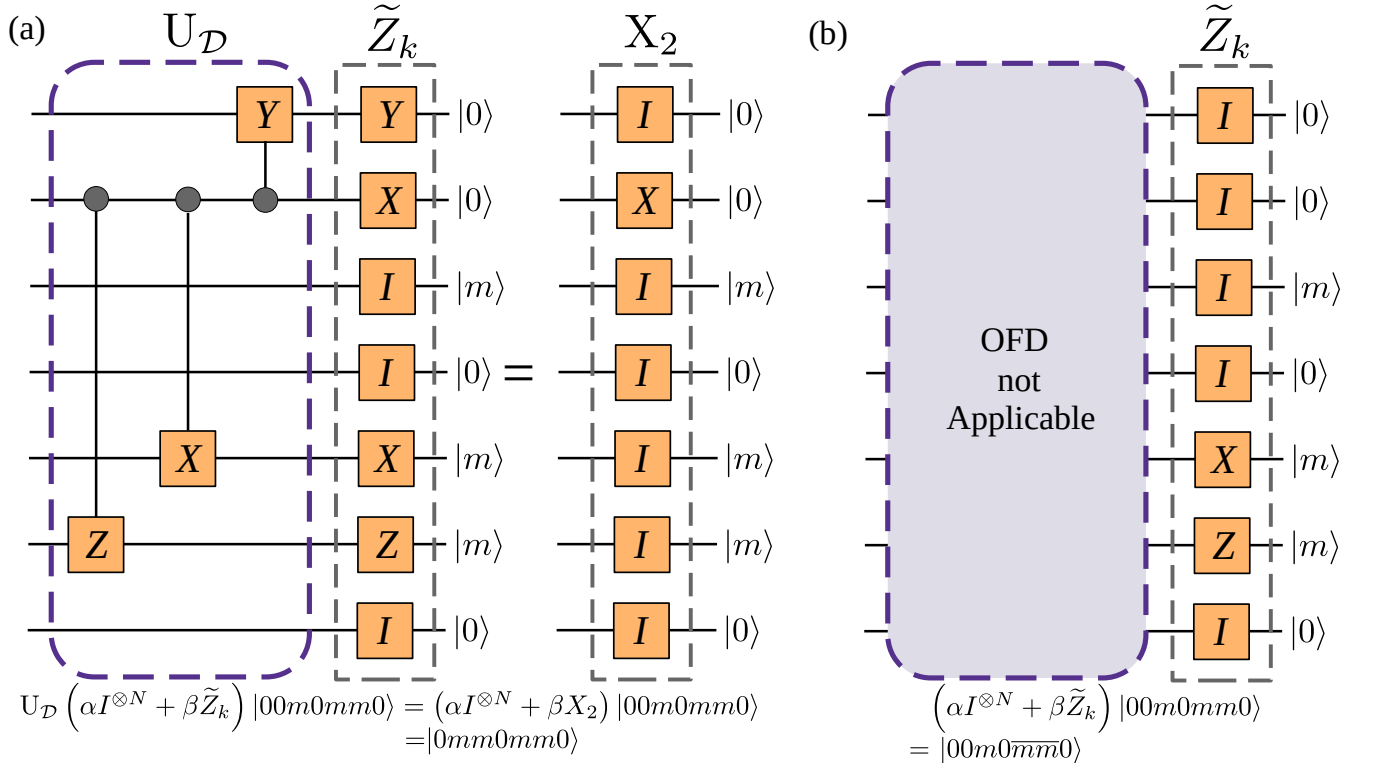


FIG. 2: Schematic diagram for the optimization-free disentangling algorithm (for  $N = 7$  qubits). (a) for  $\tilde{Z}_k = YXII XZI$  applying to  $|00m0mm0\rangle$ , choosing the second qubit as the control qubit, and constructing the appropriate disentangling circuit  $U_{\mathcal{D}}$  maintain the initial state as a product state. (b)  $\tilde{Z}_k = YXII XZI$  have multiple non-trivial Pauli terms on  $|m\rangle$  but none on  $|0\rangle$ , OFD does not apply in this case; the resulting state has the 5th and 6th qubits entangled.

In this example, when it comes to the second  $T$ -gate, we have:

$$P^b = (XC)_{1,2}(CX)_{1,2}P^a(CX)_{1,2}(XC)_{1,2}. \quad (8)$$

Thus, considering just the first two operators from  $P$ , we can see that the disentangling procedures for  $P^{a/b}$  lead to the same outcome. For instance, if  $P^a = XXII \dots I$ , then  $P^b = XIII \dots I$ , and in both cases, applying OFD results in  $|\psi_3\rangle = |mm00 \dots 0\rangle$ . Likewise, for the remaining 15 possible combinations of Pauli operators on the first two qubits, we will arrive at the same conclusion. In Fig. 3, we provides numerical evidence supporting our claim that the choice of control qubit does not affect the performance.

The OFD algorithm is summarized as follows:

---

**Algorithm 1** Optimization-free Disentangling Algorithm

---

**Input:**  $N$ -qubit CAMPS =  $\{U_c, |\psi\rangle\}$ ,  $N$ -qubit Pauli string  $P$  from Eq. (2).

- 1: Initialize: Disentangling Clifford circuit  $U_{\mathcal{D}} = I^{\otimes N}$ .
- 2: **for**  $n = 1, 2, \dots, N$  **do**
- 3:   **if**  $P[n] \in \{X, Y, Z\}$  **then**
- 4:      $\mathbb{A}'[n] \leftarrow P[n]\mathbb{A}[n]$     $\triangleright \mathbb{A}[n] \equiv \mathbb{A}_n$  is the  $n$ th qubit tensor in MPS.
- 5:   **end if**
- 6: **end for**
- 7: Find a control qubit  $v$ :  $|v\rangle$  is an eigenstate of Pauli operator **and**  $\mathbb{A}'[v] \neq \mathbb{A}[v]$ .    $\triangleright \mathbb{A}'[v] \neq \mathbb{A}[v]$ :  $|v\rangle$  is flipped by  $P[v]$ .
- 8: **if**  $v$  exists **then**
- 9:   **for**  $n = 1, 2, \dots, v-1, v+1, \dots, N$  **do**
- 10:     **if**  $\mathbb{A}'[n] \neq \mathbb{A}[n]$  **then**
- 11:       new gate  $c_{v,n} = \text{Control-}P[n]$  gate with  $v/n$  as the control/target qubit.
- 12:        $U_{\mathcal{D}} \leftarrow c_{v,n}U_{\mathcal{D}}$ .
- 13:     **end if**
- 14:   **end for**
- 15: **end if**
- 16:  $U_c \leftarrow U_c U_{\mathcal{D}}^\dagger$ ;  $|\psi\rangle \leftarrow U_{\mathcal{D}}(\alpha I + \beta P)|\psi\rangle$

**Output:** Updated CAMPS =  $\{U_c, |\psi\rangle\}$ .

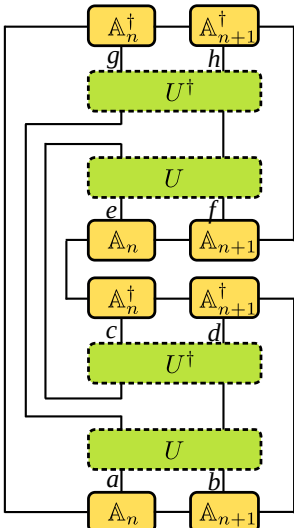
---

## B. Improved Optimization-based Disentangling Algorithm

In this section, we present the optimization-based disentangling algorithm (OBD) and describe a modification to the algorithm which results in a substantial speed-up – by several orders of magnitude over the original approach. OBD employs heuristic optimization across the entire two-qubit Clifford group. This algorithm has been utilized in the Clifford disentangling procedures from Ref. [27–32]. The main idea is to iteratively examine each pair of qubits and select the two-qubit Clifford gate that minimizes entanglement entropy over that cut. Our core modification will be a way to more efficiently compute the objective function for the optimization over all the two-qubit Clifford gates.

In OBD, the non-stabilizer component of the CAMPS is always represented by an MPS. After shifting the canonical center of the MPS between qubits  $n$  and  $n+1$ , the original OBD algorithm uses the entanglement entropy over this cut as the objective function; this entanglement entropy is computed by obtaining singular values through the singular value decomposition (SVD), with a time complexity of  $\mathcal{O}(\chi^3)$  and a memory complexity of  $\mathcal{O}(\chi^2)$  (where  $\chi$  is the MPS bond dimension), for each two-qubit Clifford gate  $U$ .

We show instead that you can compute the exponential of the second Rényi entropy using the following tensor contraction

$$\mathcal{L}(U, n) = e^{-S_2(U, n)} =$$


(9)

where  $\mathbb{A}_n$  represents the tensor for qubit  $n$  within the MPS, and  $S_2(U, n)$  denotes the second Rényi entropy at the cut of qubit  $n$  after the unitary gate  $U$  is applied to qubits  $n$  and  $n+1$ .

One can then compute  $S_2$  for all 2-qubit Clifford gates in time  $\mathcal{O}(\chi^3 + |\text{Cl}_2|)$  ( $|\text{Cl}_2| = 11,520$  is the size of the two-qubit Clifford group [33]). This can be done by first contracting the MPS tensors  $\mathbb{A}_n$  and  $\mathbb{A}_{n+1}$ , leaving physical bonds (labelled as letters  $\{a, b, c, d, e, f, g, h\}$  in Eq. (9)) uncontracted for the time being. This pre-

processing step requires  $\mathcal{O}(\chi^3)$  time and  $\mathcal{O}(\chi^2)$  memory. The resulting tensor, with  $2^8 = 256$  elements, is then dispatched to a tensor-contraction computation for each two-qubit Clifford gate  $U$ . Notably, this step has a time and memory complexity of  $\mathcal{O}(1)$ , independent of the MPS bond dimension  $\chi$ .

Overall, for sequential computation, the original method has a time complexity of  $\mathcal{O}(|\text{Cl}_2|\chi^3)$ , while the improved version achieves  $\mathcal{O}(\chi^3 + |\text{Cl}_2|)$ . If parallel computation is employed for each two-qubit Clifford gate  $U$ , the memory cost for the original method is  $\mathcal{O}(|\text{Cl}_2|\chi^2)$ , while this improved version reduces it to  $\mathcal{O}(\chi^2 + |\text{Cl}_2|)$ .

Finally, the OBD is completed by sweeping over MPS bonds from qubit 1 to  $N$ , identifying the optimal Clifford gate for each qubit pair. These sweeps continue until convergence, resulting in a disentangling Clifford circuit  $U_{\mathcal{D}}$  in a stair-step pattern.

## C. Connection between OFD and OBD

In Sec. II A, we demonstrated that OFD disentangles by identifying a control qubit and using (long-range) control-Pauli gates to flip any other targeted qubits. Meanwhile, OBD iteratively sweeps over qubit bonds, applying nearest-neighbor two-qubit gates to minimize entanglement entropy (Sec. II B). Here we show that often there is a constructive set of gates that can be chosen in the stair-step pattern of qubits that are considered by OBD which converts at most one  $|0\rangle$  to a magic state  $|m\rangle$  at each step thereby ensuring the same quality on the first  $t \lesssim N$   $T$ -gates as OBD. Moreover, because each such step will therefore keep the product state unentangled, OBD will find it by optimization. This gives a concrete explanation for why the entanglement doesn't increase in the first  $N$  steps of OBD.

To start, we note that while the control-Pauli  $c_{v,n}$  from Algorithm 1 may act over long distances, they can always be decomposed into a sequence of nearest-neighbor SWAP and control-Pauli gates. For instance, if  $v < n$ ,

$$c_{v,n} = \left( \prod_{j=n-2}^v \text{SWAP}_{j,j+1} \right) (\text{Control-}P[n])_{n-1,n} \left( \prod_{j=v}^{n-2} \text{SWAP}_{j,j+1} \right). \quad (10)$$

In other words, the long-range control-Pauli gate is equivalent to bringing the control and the target qubits next to each other and then applying the same control-Pauli gate to these two qubits, up to the operations of swapping the qubits back, which do not affect the overall performance.

Now, we consider a simple example. We start with that the  $\tilde{T}_k$  induced by the first  $T$ -gate is given by  $(\alpha I + \beta \tilde{Z}_k)$ , where  $\tilde{Z}_k = XIXXII \dots I$ . Note that the non-stabilizer part of CAMPS is initialized as  $|\psi_1\rangle = |0 \dots 0\rangle$ . Prior to Clifford disentangling, this yields

$|\psi''\rangle = (\alpha I + \beta P_1)|\psi_1\rangle = \alpha|00000\dots 0\rangle + \beta|10110\dots 0\rangle$ . Notice that OBD works by reducing the entanglement entropy; or more critically, if the MPS bond dimension is reduced to 1, this essentially gives the lowest entropy 0, hence OBD will select the corresponding gate for the disentangling circuit  $U_{\mathcal{D}}$  (note that there can be multiple gates leading to zero entropy). Let us give the MPS representation for  $|\psi''\rangle$ :

$$\begin{aligned} \mathbb{A}_1^0 &= (\alpha \ 0), \quad \mathbb{A}_1^1 = (0 \ \beta), \\ \mathbb{A}_2^0 &= \begin{pmatrix} 1 & 0 \\ 0 & 1 \end{pmatrix}, \quad \mathbb{A}_2^1 = \begin{pmatrix} 0 & 0 \\ 0 & 0 \end{pmatrix}, \\ \mathbb{A}_3^0 &= \begin{pmatrix} 1 & 0 \\ 0 & 0 \end{pmatrix}, \quad \mathbb{A}_3^1 = \begin{pmatrix} 0 & 0 \\ 0 & 1 \end{pmatrix}, \\ \mathbb{A}_4^0 &= (1 \ 0), \quad \mathbb{A}_4^1 = (0 \ 1), \\ \mathbb{A}_j^0 &= (1), \quad \mathbb{A}_j^1 = (0), \quad j \geq 5. \end{aligned} \quad (11)$$

Qubits 1 to 4 are entangled, with bond dimension larger than 1 for each of their MPS tensors. Now we demonstrate how to remove the entanglement or reduce the bond dimension to one, bond by bond. For the bond between the first and second qubit, we identify that applying a SWAP gate reduces the bond dimension to one, i.e.,  $\text{SWAP}_{1,2}|\psi''\rangle = |0\rangle(\alpha|00000\dots 0\rangle + \beta|11100\dots 0\rangle)$ . Next, focusing on the bond connecting the second and third qubits, we find that applying the XC gate further reduces the entanglement, i.e.,  $\text{XC}_{2,3}\text{SWAP}_{1,2}|\psi''\rangle = |00\rangle(\alpha|0000\dots 0\rangle + \beta|1100\dots 0\rangle)$ . At the next step, using  $\text{XC}_{3,4}$ , we obtain  $|\psi_2\rangle = \text{XC}_{3,4}\text{XC}_{2,3}\text{SWAP}_{1,2}|\psi''\rangle = |000\rangle(\alpha|0\rangle + \beta|1\rangle)|00\dots 0\rangle$ . Here, the fourth qubit is now a magic qubit, denoted as  $|m\rangle = (\alpha|0\rangle + \beta|1\rangle)$ . Thus, we have explicitly constructed the disentangling Clifford circuit  $C_1 = \text{XC}_{3,4}\text{XC}_{2,3}\text{SWAP}_{1,2}$  for the first  $T$ -gate, with the resulting MPS  $|\psi_2\rangle = |000m00\dots 0\rangle$ .

Furthermore, if  $|\psi\rangle$  contains some magic qubits, but is still a product state, we can likewise construct a disentangling circuit bond by bond. For instance, on the example from Fig. 2(a), we identify that  $U_{\mathcal{D}} = (\text{XC})_{1,2}\text{SWAP}_{2,3}\text{SWAP}_{3,4}(\text{CX})_{4,5}\text{SWAP}_{4,5}(\text{CX})_{5,6}$  reduces  $\tilde{T}_k|\psi\rangle$  to the product state  $|0m0mmm0\rangle$ .

We further generalize this conclusion to the cases where some magic qubits have got entangled for once. For example, assuming  $|\psi\rangle = |0\overline{m}\overline{m}\overline{m}\overline{m}00\rangle$ , where  $|\overline{m}\overline{m}\overline{m}\overline{m}\rangle = \alpha|mmm\rangle + \beta|m_X m_Y m_Z\rangle$ , and  $\tilde{Z}_k = XIIIX$ , we have  $|\psi'\rangle = \alpha|0\overline{m}\overline{m}\overline{m}\overline{m}00\rangle + \beta|1\overline{m}\overline{m}\overline{m}\overline{m}01\rangle$ . Applying  $\text{SWAP}_{1,2}$  will not change the entanglement entropy over cut between qubits 1 and 2, however, there are no two-qubit Clifford gates that are able to reduce the entropy generically, hence OBD can pick  $\text{SWAP}_{1,2}$  over this bond. Similarly,  $\text{SWAP}_{2,3}$  will be picked as it keeps the entropy the same and no other gates can reduce the entropy. Next,  $\text{SWAP}_{3,4}$  and  $\text{SWAP}_{4,5}$  reduce the entropy to 0, and will be picked by OBD. At last,  $\text{CX}_{5,6}$  completes the search of disentangling circuit and results in the final state  $|\psi\rangle = |0\overline{m}\overline{m}\overline{m}\overline{m}0\rangle$ .

However, there is one situation where OBD does not necessarily reproduce the OFD algorithm: if magic

qubits become entangled more than once, the above arguments break down, as the SWAP gate increases the entropy, violating the criteria for OBD to select it as a disentangling gate. In such cases, OFD outperforms OBD by bypassing the entangled magic qubits and employing long-range control-Pauli gates to reduce the entropy of the initial state. Nevertheless, for the random circuits considered in this work, such scenarios seem to be rare, and we observe comparable performance between OFD and OBD.

The classical simulatability of CAMPS is primarily determined by the non-stabilizer component that is represented with the MPS, for which we assess the memory and computational complexity through the maximal bond dimension and second Rényi entanglement entropy  $S_2$  as the bond-dimension scales exponentially with the entanglement, i.e.,  $\chi \propto e^{S_2}$ . The Clifford part can be managed efficiently with  $\mathcal{O}(N^2)$  integer numbers and  $\mathcal{O}(N^3)$  operations for an  $N$ -qubit system using a stabilizer tableau.

In Fig. 3, we show that OFD achieves comparable results to OBD when simulating  $t$ -doped Clifford circuits, effectively matching OBD in second Rényi entropy  $S_2$  (the maximal value over all the cuts within the MPS), maximal bond dimension, and nullity  $\nu$  (i.e., the number of magic qubits, see Appendix D for our improved stabilizer group learning algorithm) of the MPS component  $|\psi\rangle$  up until all qubits become magic. During this stage, OFD relies on SWAP and control-Pauli gates to distill non-stabilizerness by leveraging non-magic qubits. However, once all qubits are magic, we stop doing any disentangling in OFD resulting in slightly elevated entropy and bond dimension compared to OBD. Because OFD and OBD are essentially identical, we use OBD for most of the data shown in the rest of the paper unless noted otherwise.

As shown in Fig. 4, for CAMPS with Clifford disentangling, the MPS entanglement entropy  $S_2$  averaged over several circuit realizations remains almost 0 until  $t \simeq N$ . For comparison, we also include results from MPS and CAMPS without Clifford disentangling, showing that adding a Clifford circuit on top of MPS reduces the entanglement significantly, and Clifford disentangling is crucial as well to keeping the stabilizer and non-stabilizer components separated and minimizing the entanglement within the MPS component.

Moreover, we present the stabilizer nullity (i.e., the number of magic qubits) of CAMPS as a function of  $T$ -gate number in Fig. 5. In the average case (over a number of random circuit realizations), the nullity obeys a simple function form across a wide range of system sizes:

$$1 - \frac{\nu}{N} = \begin{cases} 1 - \frac{t}{N} & t \leq N, \\ 0 & t > N. \end{cases} \quad (12)$$

showing that as expected one  $T$ -gate turns one qubit into a magic qubit. For individual circuit realization, as shown in Fig. 3(c), the nullity changes by at most one

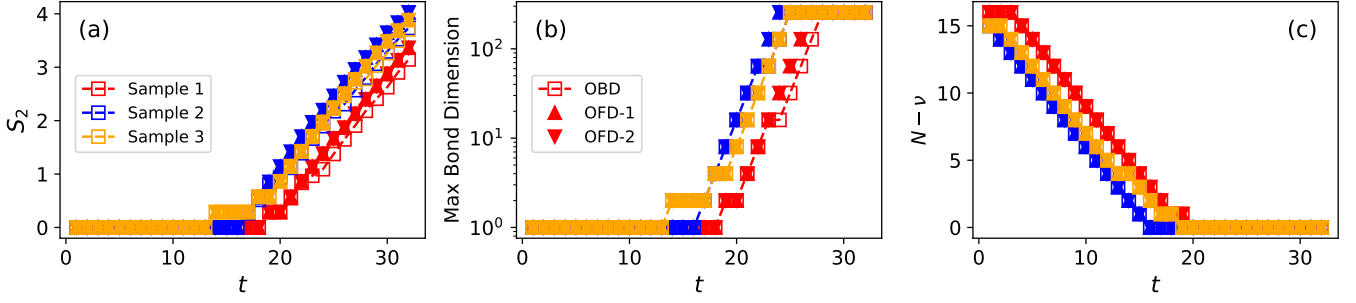


FIG. 3: Results of applying various types of Clifford disentangling algorithms (symbols) to different samples of CAMPS (colors) from the simulation of  $t$ -doped Clifford circuits ( $N = 16$ ,  $N_T = 1$ ): (a) the second Rényi entropy of the MPS piece of CAMPS; (b) the maximal MPS bond dimension of CAMPS; (c) the nullity  $\nu$  of the CAMPS.

Symbols are CAMPS from (OBD) OBD disentangling algorithm (Sec. II B); and (OFD-1 and OFD-2) OFD disentangling algorithm with two choices of control qubits (Sec. II A)

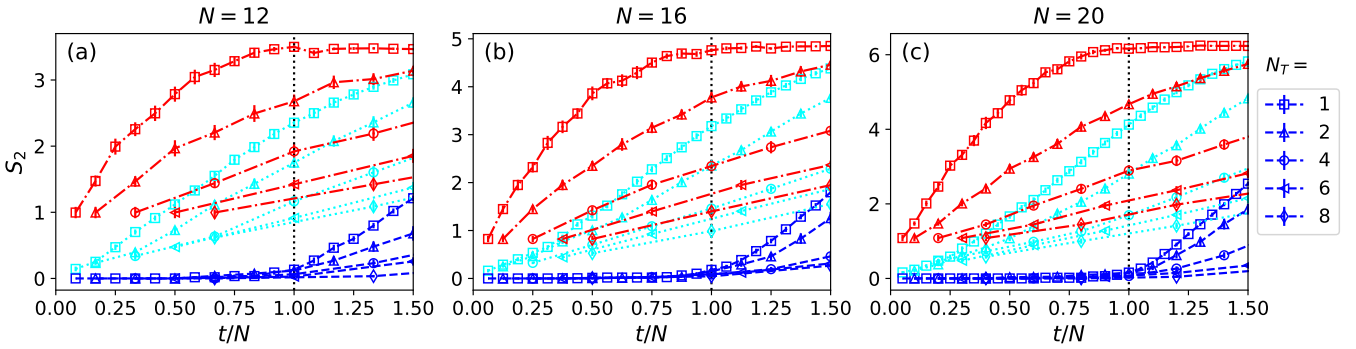


FIG. 4: The MPS second Rényi entropy from the simulation of  $t$ -doped Clifford circuits using MPS (red), CAMPS with OBD Clifford disentangling (blue) and CAMPS without Clifford disentangling (cyan) for various choices of system size  $N \in \{12, 16, 20\}$  and  $T$  gate number per layer  $N_T \in \{1, 2, 4, 6, 8\}$ . Each data is averaged over 16 circuit realizations and error bars are present.

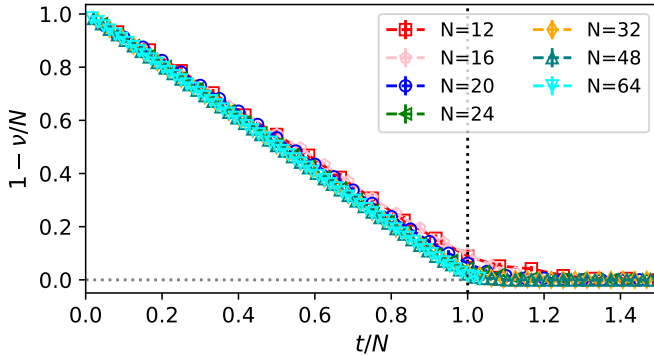


FIG. 5: Stabilizer nullity  $\nu$  of CAMPS as a function of the number of  $T$ -gates  $t$  ( $N_T = 1$ ) for various  $N$ . Each nullity data is averaged over 16 circuit realizations with error bar present.

for each non-Clifford  $T$ -gate, which is consistent with the mechanism of OFD.

We also consider various other distributions of circuits.

For instance, in Fig. 6, we consider two scenarios: (a) distributing the  $T$ -gates only among the first  $n_r$  qubits, and (b) using the same two-qubit Clifford gate throughout the entire circuit. In both of these cases, we see essentially qualitatively the same behaviors as in the random Clifford case.

We also consider higher-dimensional circuit architectures, where we continue to use MPS to represent the non-stabilizer components of the quantum states, as it allows efficient manipulation of the canonical center and minimizes bipartite entanglement by focusing only on nearest-neighbor qubit pairs. Importantly, the essential steps in this simulation – such as absorbing Clifford gates into the stabilizer tableau and commuting the non-Clifford gates through the Clifford circuits (Appendix. B) – maintain the same computational complexity regardless of gate locality. This enables CAMPS to effectively represent  $t$ -doped Clifford circuits of arbitrary geometries. In Fig. 7, we verify that CAMPS remains as an efficient representation for 2D circuits by showing that the MPS entropy displays a similar trend to the 1D case.

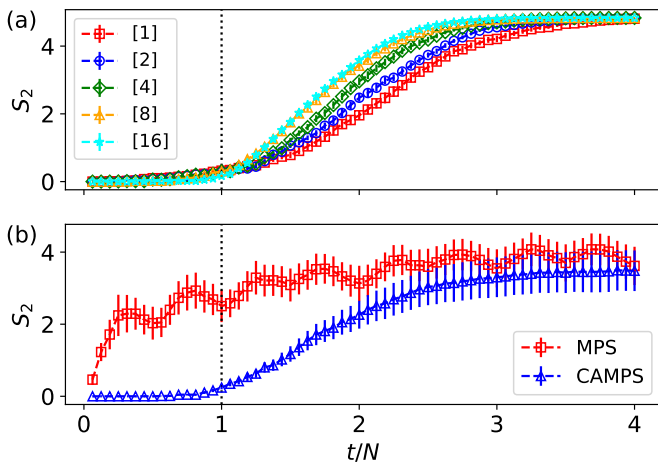


FIG. 6: The MPS second Rényi entropy from the simulation of  $t$ -doped Clifford circuits with specific restrictions. (a) The positions of  $T$  gates are distributed among the first  $n_r$  qubits. Results are shown for  $n_r \in \{1, 2, 4, 8, 16\}$  with  $N = 16$ ,  $N_T = 1$ . (b) All the two-qubit gates are identical for the whole circuit. Each data is averaged over 16 circuit realizations and error bars are present.

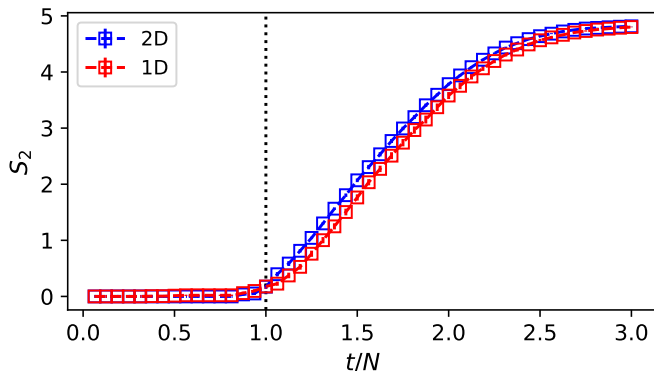


FIG. 7: The MPS second Rényi entropy from the CAMPS representing 2D  $t$ -doped Clifford circuits ( $N = 4 \times 4$ ,  $N_T = 1$ , averaged over 16 circuit samples). Results of 1D circuits (from Fig. 4) are also shown for comparison.

### III. CAMPS FOR $(t \leq N)$ -DOPED CLIFFORD CIRCUITS

The numerical results from previous section have suggested that, on average, CAMPS with Clifford disentangling algorithms provides an efficient representation for random  $(t \leq N)$ -doped Clifford circuits. In this section, we provide further analysis on this observation.

OFD guarantees that the entanglement does not increase for the twisted Pauli string  $\tilde{Z}_k$  which has a non-trivial Pauli term on a  $|0\rangle$  qubit. In such a case, that

qubit will be ‘consumed’ and turned into a magic state; we therefore call the  $T$ -gate that gives rise to this Pauli string as a free  $T$ -gate. Otherwise, the entanglement may increase (in the worse case doubling the bond-dimension) but no  $|0\rangle$  qubit is affected; we refer to these  $T$ -gates as entangling  $T$ -gates.

To understand the question of simulatability of  $t$ -doped circuits with  $t = N$ , we need to understand whether there are a sufficient number of free  $T$ -gates within the first  $N$  such gates - i.e. a situation where  $N/2$   $T$ -gates are not free would still result in exponential complexity for the classical simulation. It is worth pointing out that the relevant Pauli-strings for OFD are  $\tilde{Z}$  which are commuted through both the circuit and disentanglers up to this point in the algorithm.

That said, let us first consider just the twisted Pauli-string  $\tilde{Z}$  generated from a  $T$ -gate commuted through the circuit (but not any disentangler), i.e.,

$$|\Psi\rangle = U_C \prod_{j=t}^1 \left( \alpha I + \beta \tilde{Z}^{[j]} \right) |0\rangle^{\otimes N} \quad (13)$$

Such a Pauli-string will be non-identity on a window of qubits whose width is caused by the induced light-cone and is equal to the circuit depth of the  $T$ -gate. It will behoove us to consider then the effect of  $T$ -gates at different depths and therefore the widths of twisted Pauli strings. Within this ‘width’  $w$  there will be some distribution of Pauli terms. To reason about this, we start by considering the situation where this distribution is uniform over all  $4^w$  Pauli strings. We now must consider the effect on that distribution from commuting these strings through the relevant disentanglers, i.e.,

$$\tilde{Z}^{[j]} = \left( \prod_{j'=1}^{j-1} U_D^{[j']\dagger} \right)^\dagger \tilde{Z}^{[j]} \left( \prod_{j'=1}^{j-1} U_D^{[j']\dagger} \right) \quad (14)$$

where  $U_D^{[j']}$  is the disentangling Clifford circuit for  $j'$ -th  $T$ -gate, such that

$$|\Psi\rangle = U_C \left( \prod_{j=1}^t U_D^{[j]\dagger} \right) \prod_{j=t}^1 \left[ U_D^{[j]} \left( \alpha I + \beta \tilde{Z}^{[j]} \right) \right] |0\rangle^{\otimes N} \quad (15)$$

In the limit where  $w = N$ , the distribution is invariant as any Clifford operator is a one-to-one mapping between Pauli strings. In fact, even in the case where  $w < N$ , one can show that for any qubit (or window of qubits) which are uniformly distributed over Pauli strings, they map to a uniform distribution on that same window while potentially including other Pauli terms outside that window; this helps ensure that uniformity of the distribution prior to the disentanglers is preserved after commuting through them.

Let us start by considering  $T$ -gates whose depth is linear in the system size and therefore Pauli strings that

span the whole system. In such a situation, the probability for turning one qubit into magic, if there are already  $N_m$  qubits in magic states, goes as

$$p(N_m) = 1 - \left(\frac{1}{2}\right)^{N-N_m}, \quad N_m = 0, 1, 2, \dots, N-1 \quad (16)$$

which is the probability for  $\tilde{Z}$  having at least one non-trivial Pauli term on the non-magic qubits, such that OFD is applicable and one of these qubits become magic after disentangling. The expected number of Pauli strings to find a usable control qubit is  $1/p(N_m)$  and therefore, the overall average number of Pauli strings needed to consume all the  $N$  free qubits is given by

$$t_{\text{free}} = \sum_{N_m=0}^{N-1} \frac{1}{1 - \left(\frac{1}{2}\right)^{N-N_m}} \quad (17)$$

from which, we have (see Appendix C for the derivation)

$$N + 1 - \frac{1}{2^N} < t_{\text{free}} < N + 2 - \frac{1}{2^{N-1}}, \quad \forall N \quad (18)$$

In other words, (in expectation) all but a constant number of  $T$ -gates amongst the first  $N$  gates are free. Note that this expectation is an upper bound; in fact, we ignored the probability for  $\tilde{Z}$  being a trivial Pauli string, i.e., with  $I/Z$  on the non-magic qubits in  $|0\rangle$ , and  $I$  on the magic qubits, which would not require any disentangler; nonetheless, this will have only a small effect on this upper bound as this latter probability is small  $((1/2)^{N-N_m} (1/4)^{N_m})$  compared to  $p(N_m)$ .

In cases where the window-size is smaller, it is harder to directly analytically reason about the number of entangling gates in the first  $N$   $T$ -gates. Instead, we numerically model the OFD algorithm. Here we assume that once a  $|0\rangle$  has been consumed and turned into a magic state it is no longer usable as a control qubit; while this is generically true it is a slight under-count because occasionally a magic qubit can be turned into a free qubit again. For windows that do not span the system, the location of the windows are important. Here we start by considering the case where all  $N$  windows are the same size and centered on a randomly chosen (but without replacement) qubit that the  $T$ -gates act on. We show in Fig. 8(a) that the number of entangling gates grows linearly with system size for a fixed window-size  $w$  with a slope (see Fig. 8(b)) which decays exponentially with  $w$ . Therefore, if we choose a window size  $w$  (and therefore a depth  $2w$  of  $T$ -gates) which scales at least as  $w \propto \log(N)$  the number of entangling gates should scale sublinearly; in fact, we see from Fig. 9 that the number of entangling gates scales logarithmically or sub-logarithmically with  $N$ . Windows of size larger than  $\log(N)$  are only helpful as one can always use the control qubits as if one has access to a smaller window. We also see that the distribution is tightly centered around the expectation suggesting that the typical circuit matches the average

circuit. A logarithmic number of entangling  $T$ -gates can always be dealt with in polynomial time as the bond-dimension of CAMPS scales at most exponentially in the number of such gates. In Fig. 11, we present the numerical results for representing the  $t$ -doped Clifford circuits with CAMPS using OFD. The circuits have all the first  $N$   $T$ -gates on the  $L_T$ -th layer. From Fig. 11(a), we observe that  $S_2$  starts increasing when  $t \approx 0.9N$  for  $w = 2L_T > \log(N)$ , which, along with the  $S_2$  displayed in Fig. 11(b-d) for individual circuit samples, indicate only a small number of entangling  $T$ -gates exist for  $w > \log(N)$ . However, for  $T$ -gates of depth smaller than  $\log(N)$  (i.e constant depth) there are too many entangling gates; therefore, naively, one might expect if one has a large number of  $T$ -gates at constant depth, this would be problematic. It turns out that in one-dimensional circuits this is not the case.

For an MPS, though, every layer of local gates can only double the bond-dimension and so the bond-dimension will still be polynomial after  $\log(N)$  layers. CAMPS has the property that it is using an MPS and disentangling it with Clifford gates and so (up to the quality of the disentangling), CAMPS also will have an MPS bond-dimension that only scales polynomially after  $\log(N)$  layers as in the “worst-case” CAMPS just uses the inverse of the Clifford circuit as the disentangler to remove any Clifford piece. Therefore, we are left in a situation where for one-dimension the  $T$  gates on the first  $\log(N)$  layers do not matter and uniformly distributed  $T$  gates (up to  $N$  such gates) on layers above  $\log(N)$  can be dealt with efficiently using OFD. In two-dimensions, this is no longer true and generically two-dimensional circuits with more than  $\log(N)$   $T$ -gates on constant-depth may not be simulatable efficiently but all the  $T$ -gates above logarithmic depth can be.

We can also consider a distribution of window locations which has some non-uniformity. For example, consider  $T$ -gates distributed over two layers at depth  $w$  and  $w+1$  where the  $T$ -gates on each layer are uniformly distributed over  $N/2$  qubits on that layer. In such a case, there will be an extensive number of twisted Pauli strings that are centered on the same qubit. Here (see Fig. 8(c)) we still find that the number of entangling gates scales linearly with systems size at a fixed window  $w$  but with a slope which now decays exponentially in  $\sqrt{w}$  (see Fig. 8(d)); this means that we need  $T$ -gates at depth (and hence window-size) at least proportional to  $\log^2 N$ . If we then use MPS to absorb all the  $T$ -gates up to this depth we get a simulation which is only quasi-polynomial in system size.

In the limit where uniformity of  $T$ -gates is strongly violated, we can see that our simulation techniques break down. Consider the case where the windows from all  $N$   $T$ -gates actually span only a sub-linear number of  $k$  qubits. In such a case, this is equivalent to running on a circuit of  $k$  qubits and we will not achieve more than  $k$  free  $T$ -gates as there are only  $k$   $|0\rangle$  to consume. It is worth pointing out that this “uniformity” requirement is

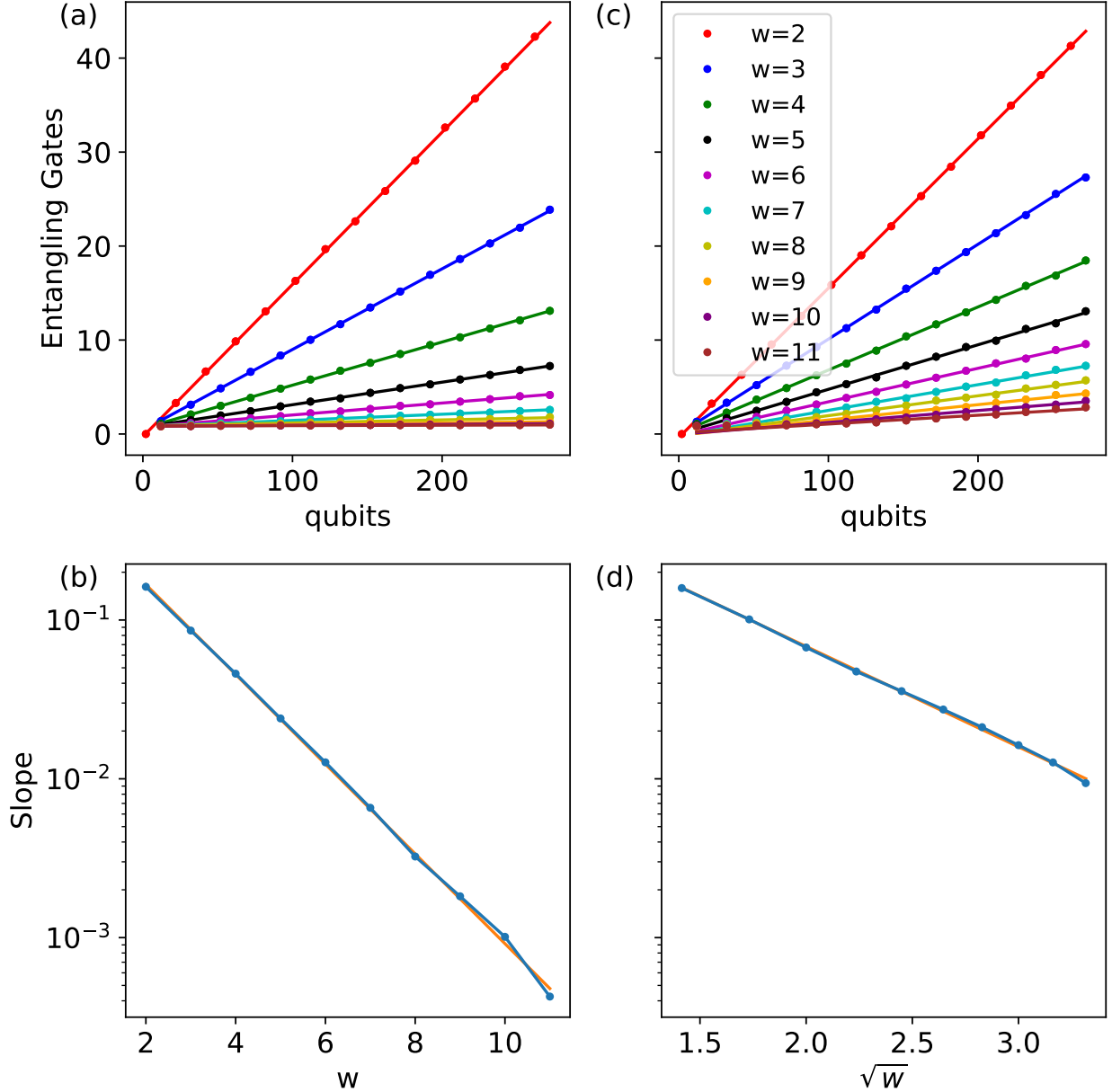


FIG. 8: Expected number of entangling gates versus number of qubits  $N$  for OFD being applied to a model of random twisted Pauli strings  $\bar{Z}$  for (a) a set of  $N$  windows of size  $w$  and (c) two sets of  $N/2$  windows of size  $w$  and  $w + 1$  respectively. Error bars are below the size of dots. The lines are best-fit to all but the first five data points. Windows within each set are centered on unique qubits. (b,d) Slopes of (a) and (c) versus  $w$  and  $\sqrt{w}$  respectively.

on the location of the Pauli-string windows and so  $T$ -gates that are all to the left-half of the system but at varying depths still are likely to be sufficiently uniform in window-location given the spread of the light cone.

In our simplified model, we've been using an assumption that the Pauli strings are uniformly distributed. In practice, this model is not fully realistic. For example, in Fig. 10 we can see that in the window size induced by the light-cone where Pauli strings can be supported,

there is significantly less non-identity Pauli terms at the edge of the window than in the center for a prototypical example on a random Clifford circuit. It is an interesting open question whether there are more realistic models of Pauli string distributions that are applicable to different distributions of circuits.

In summary, we find that in one-dimension for relatively uniform distribution of up to  $N$   $T$ -gates we have a simulation that is at most quasi-polynomial. In two-

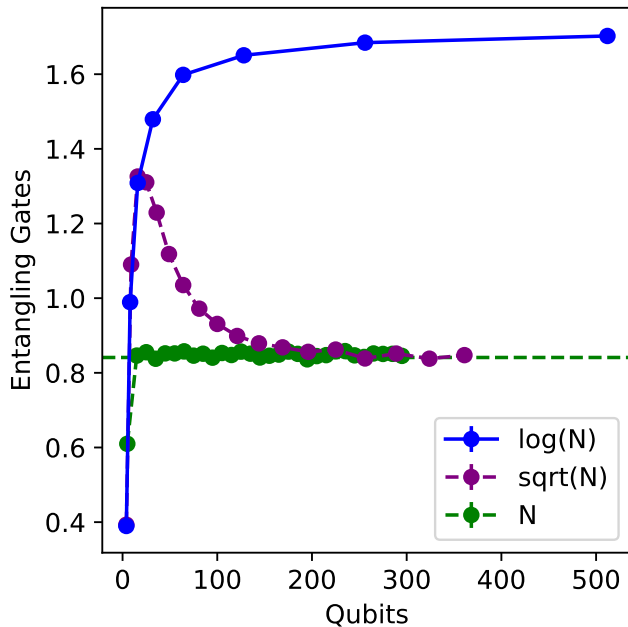


FIG. 9: Expected number of entangling gates as a function of qubits  $N$  for  $N$  different windows of size  $w$  where  $w$  scales as in the legend and where each window is centered on one of the  $N$  qubits.

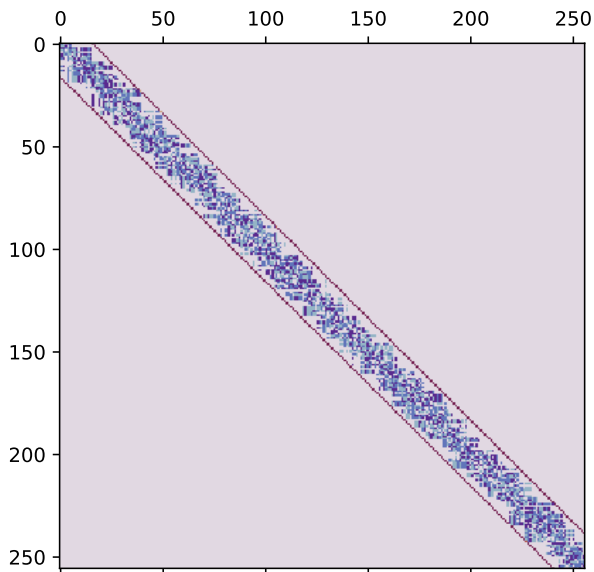


FIG. 10: Prototypical example of a distribution of Pauli-strings coming from the 256 Pauli terms on 256 qubits with  $N = 256$   $T$ -gates uniformly located at depth  $\log 256 = 8$  (so that  $w = 16$ ). White corresponds to identity terms with other colors corresponding to  $X, Y, Z$ . The red lines show the maximum window size that the Pauli-terms can be located on.

dimension, we can achieve a polynomial simulation up to  $N$  doped  $T$ -gates as long as those  $T$  gates are at least logarithmically deep; in fact, a constant  $T$ -gates per layer before logarithmic depth (or a logarithmic number of  $T$ -gates total) will also be simulatable in polynomial time.

#### IV. CAMPS FOR $(t > N)$ -DOPED CLIFFORD CIRCUITS

In this section, we explore the simulation for  $t > N$  for various random circuit distributions. First, we consider distributions with  $L_T = 1$  for various  $N$  and  $N_T$  (see Fig. 1); later in this section we will consider distributions with fixed  $N$  and various combinations of  $(L_T, N_T)$ .

##### A. Random $t$ -doped Clifford Circuits with $L_T = 1$

In Fig. 4, we observe that the simulation with MPS alone (without Clifford augmentation) reaches the maximal entanglement at circuit depth  $\simeq N$  as expected. However, using CAMPS postpones the saturation significantly, even without the Clifford disentangling as the CAMPS still transfers some entanglement to the Clifford piece. The main effect of disentangling seems to primarily be that the first  $\approx N$   $T$  gates do not increase the entanglement but the rate of entanglement growth after this seems to be similar. In Fig. 12, we plot  $S_2$  as a function of the  $T$ -gate number  $t$  for system sizes up to 64. We observe that CAMPS reaches the maximal entanglement at  $t \simeq 2.5N$  with the MPS entanglement dynamics collapsing across system sizes. We find that  $S_{2,\max}$  scales linearly as  $S_{2,\max} \simeq 0.356N - 0.878$  by fitting the maximum  $S$  for  $N \leq 20$  where we can simulate the  $t$ -doped Clifford circuits using CAMPS without bond truncation; we extrapolate this to determine  $S_{2,\max}$  for  $N > 20$  where truncation prevents us from getting the exact result at large number of  $t$  gates (see inset of Fig. 12). Interestingly, the  $S_2$  of the truncated MPS diverges from the expected behavior when the norm of the MPS component [34, 35],  $\tilde{F} = |\langle \psi | \psi \rangle|^2 \approx e^{-1}$ . Once bond truncation is introduced, the benefits of Clifford disentangling diminish. This is because the bond truncation discards small singular values in the MPS; additional entangling gates from Clifford disentangling introduce new small singular values, leading to alternating cycles of bond truncation and distillation that degrade the fidelity of the CAMPS by continuously discarding these tails. Therefore, we cease Clifford disentangling once bond truncation begins.

We now consider the MPS entanglement Rényi entropy as we change the number of  $T$  gates per layer for different system sizes (see Fig. 13(a)). We find the entropy data collapses by rescaling  $t$  as

$$\tilde{t} = \begin{cases} t - N & t \leq N, \\ \frac{1}{t_s}(t - N) & t > N. \end{cases} \quad (19)$$

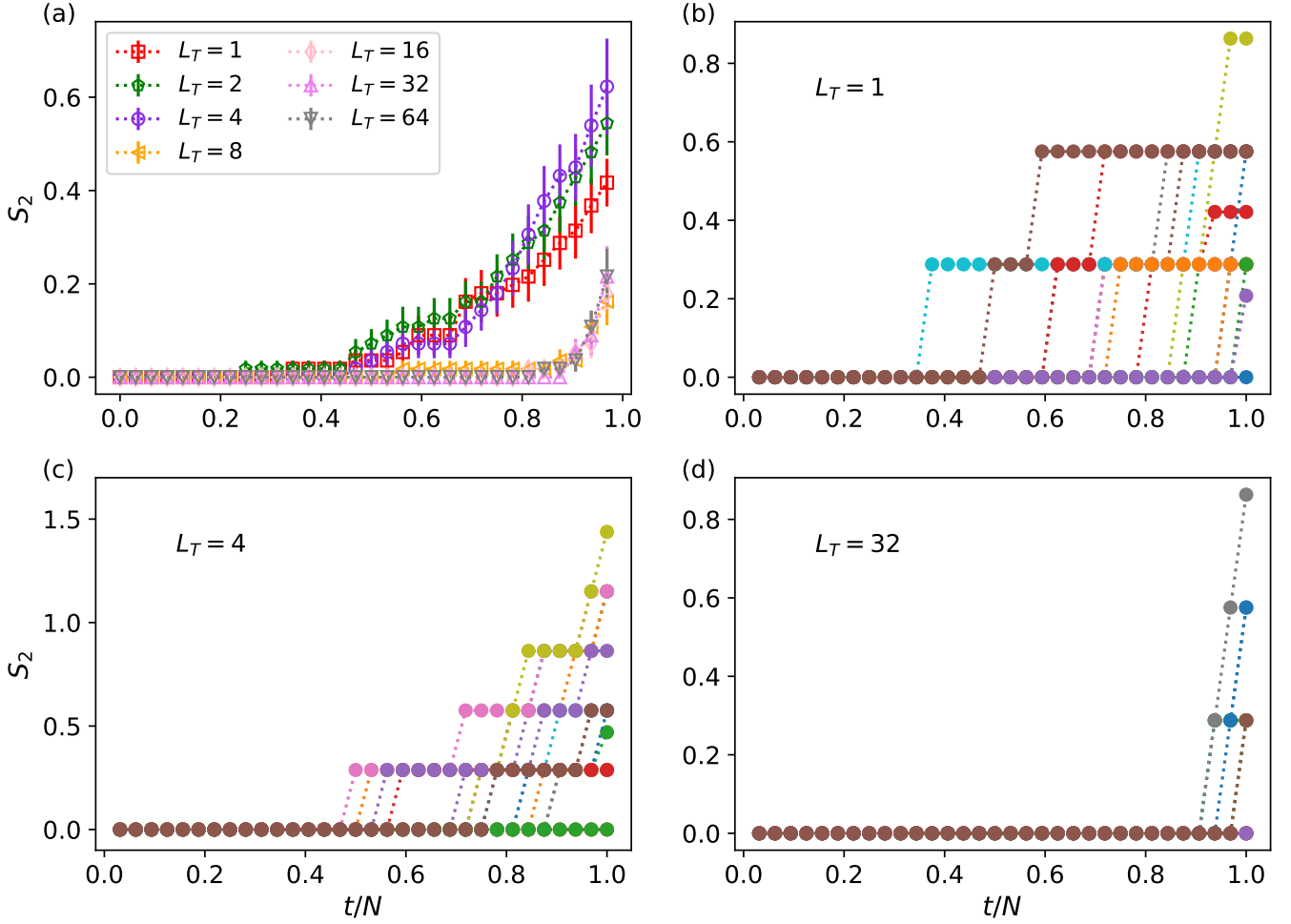


FIG. 11: The MPS second Rényi entropy from the simulation of 1D  $t$ -doped Clifford circuits with CAMPS ( $N_T = N = 32$ ). (a)  $S_2$  averaged over 16 random circuits for various  $L_T$ ; (b)-(d)  $S_2$  from individual circuit realizations. The  $T$ -gates from the same layer are absorbed into CAMPS in random order.

where  $t_s$  is the average over  $N$  of the number of  $T$ -gates (not including the first ‘free’  $N$   $T$ -gates) needed to increase the MPS entropy from 0 to the maximum scaled by  $1/N$ . We find (see Fig. 13(b)) that  $t_s \approx N_T$  with a slight deviation for  $N_T = 1$  suggesting that, for  $L_T = 1$  circuits, a unit increase in entanglement happens after every  $N_T$  gates or one layer.

### B. Random $t$ -doped Clifford Circuits for various $(L_T, N_T)$

Now, we fix the qubit number  $N = 16$ , and tune the values of  $N_T$  and  $L_T$ . We observe that

1. In Fig. 14(b), when  $L_T = 1$ ,  $S_2$  has the same rate of growth per layer for  $N_T > 1$ , while  $N_T = 1$  displays obvious deviation.
2. In Fig. 14(a), when  $N_T = 1$ ,  $S_2$  has the same rate of growth per  $T$ -gate, regardless of the number of

Clifford layers  $L_T$ .

3. In Fig. 14(a), when  $N_T > 1$ ,  $L_T$  affects  $S_2$  increment per  $T$ -gate in a non-trivial way, for example, the rate of  $S_2$  growth per  $T$ -gate for  $(L_T, N_T) = (2, 2)$  is close to that of  $(L_T, N_T) = (1, 1)$ , and  $(L_T, N_T) = (4, 4)$  is close to  $(L_T, N_T) = (1, 2)$ .

We also show in Fig. 15 the distribution of  $\Delta S_2$  – the amount  $S_2$  changes from each  $T$ -gate – before  $S_2$  reaches the maximum. We observe where the group of  $(L_T, N_T)$  collapse that there is similar probability distribution of  $\Delta S_2$ . We also observe that as  $N_T$  increases (i.e., more  $T$ -gates are placed in one layer), more  $T$ -gates contributes zero increased entropy to the MPS component. It remains as an open question regarding why  $L_T$  and  $N_T$  together affect the MPS entanglement entropy in such an intriguing way and we leave it for future work.

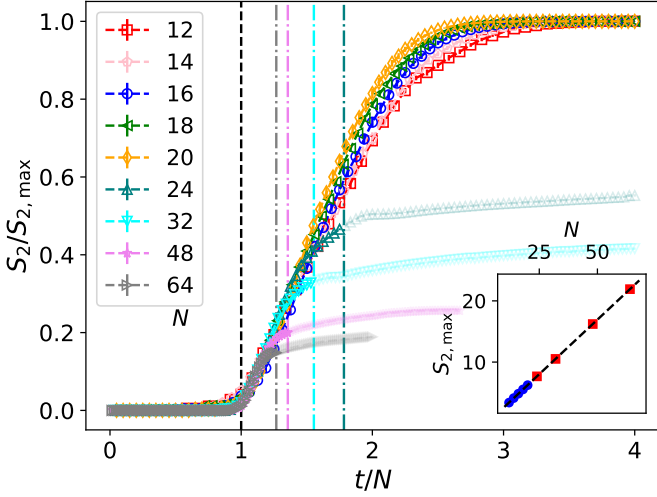


FIG. 12: The MPS second Rényi entropy of CAMPS over  $S_{2,\max}$  as a function of the number of  $T$  gates over  $N$   $t/N$  with  $N_T = 1$ . Each data point is averaged over 16 circuit realizations with error bars included. Black dashed vertical line: position of  $t/N = 1$ ; dashdot vertical lines: positions of  $t/N$  at which  $\tilde{F}$  for each  $N$  reduces to  $e^{-1}$ . Inset: linear fit to  $S_{2,\max}$  as a function of  $N$ : blue circles: the exact values for  $N \leq 20$ ; dashed line: linear fitting to the exact values; red squares: estimation of  $S_{2,\max}$  from the fitting line for  $N > 20$ .

## V. SIMULATION TASKS

We have demonstrated that CAMPS provides a compact representation for the quantum states from  $t$ -doped Clifford circuits with  $t \lesssim N$ . However, to accomplish the classical simulation, it is necessary to be able to obtain useful information from the CAMPS states. Given the access to CAMPS, it is straightforward to evaluate the expectation values of Pauli strings (see Appendix G for the numerical results). In addition, we have showed the stabilizer nullity of CAMPS using a polynomially efficient algorithm (see Appendix D). In this section, we present the algorithms for the following tasks: (1) the probability calculation or the sampling of bitstrings, computation of (2) the amplitude of bitstrings and (3) the entanglement Rényi entropy of the entire CAMPS states.

### A. Probability and Sampling of Bitstring

We leverage the methods introduced in Sec. II to efficiently sample bitstrings from CAMPS states or compute the probability of any given bitstring. In this context, measurements are replaced with projection operators:

$$P^{[0]} = |0\rangle\langle 0| = \frac{1}{2}I + \frac{1}{2}Z, \quad P^{[1]} = |1\rangle\langle 1| = \frac{1}{2}I - \frac{1}{2}Z. \quad (20)$$

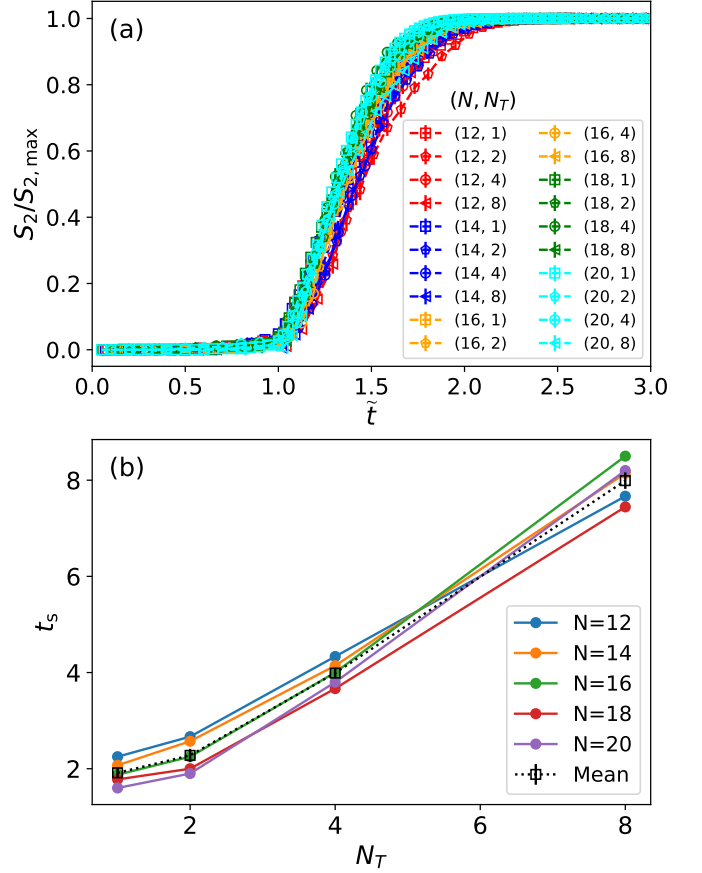


FIG. 13: (a) The MPS second Rényi entropy  $S_2/S_{2,\max}$  as a function of the rescaled  $t$ , for  $(N, N_T) \in \{12, 14, 16, 18, 20\} \times \{1, 2, 4, 8\}$ . (b) Scaling factor for  $t$  as a function of  $N_T$ . Each data is averaged over 16 circuit realizations, with error bars included.

For a CAMPS  $U_C|\psi\rangle$ , we commute the Pauli strings through the Clifford circuit part and absorb them into the MPS part:

$$P_k^{[0]}U_C|\psi\rangle = U_C \left[ \left( \frac{1}{2}I + \frac{1}{2}\tilde{Z}_k \right) |\psi\rangle \right] = U_C|\phi\rangle \quad (21)$$

where Clifford disentangling can be applied to  $|\phi\rangle = \left( \frac{1}{2}I + \frac{1}{2}\tilde{Z}_k \right) |\psi\rangle$  to reduce the bond dimension. The marginal probability of the  $k$ -th qubit is then given by

$$\pi(s_k = 0) = \langle \psi | U_C^\dagger P_k^{[0]} U_C | \psi \rangle = \langle \phi | \phi \rangle \quad (22)$$

Before we move on to the next qubit, we update the CAMPS with the new state  $|\Psi\rangle = P_k^{[0]}U_C|\psi\rangle$ . Repeating this process for all the qubits yields the probability for a bitstring  $\mathbf{s} = (s_1, s_2, \dots, s_N)$  as

$$\text{Prob}(\mathbf{s}) = \pi(s_0)\pi(s_1|s_0)\dots\pi(s_N|s_{1:N-1}) \quad (23)$$

Additionally, we can sample the 0/1 state at each site  $k$  using the marginal probability on  $k$ -th qubit. The procedures for these two algorithms are outlined in Algorithm 2 and Algorithm 3, respectively.

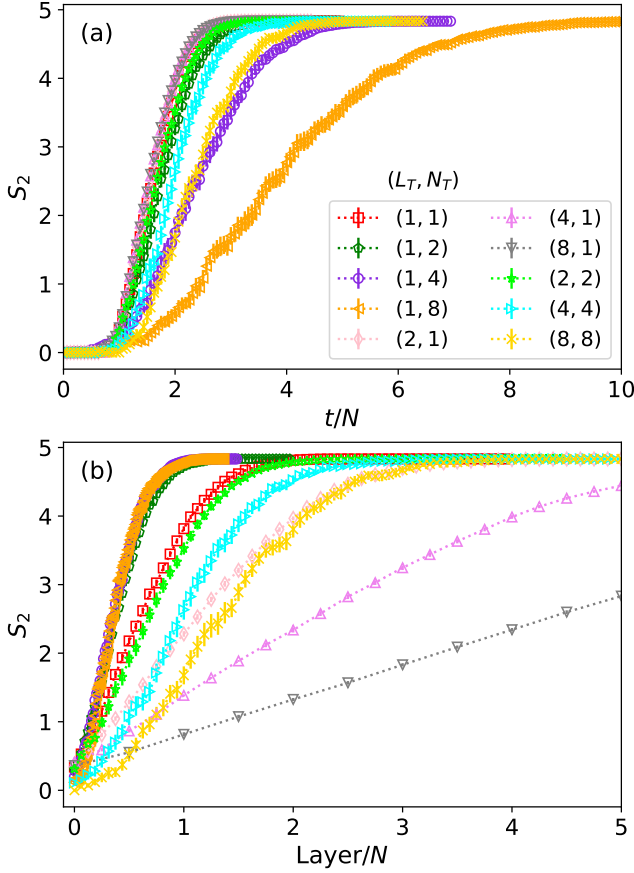


FIG. 14: The MPS second Rényi entropy  $S_2$  as a function of (a)  $t/N$  and (b) the circuit layer over  $N$  after  $N = 16$   $T$ -gates have been applied, for various values of  $(L_T, N_T)$ , i.e.,  $\text{Layer} = L_T \cdot (t - N)/N_T$ . The data are averaged over 16 circuit realizations, with error bars included.

---

### Algorithm 2 Bitstring Probability from Clifford-MPS

---

**Input:** Clifford-MPS  $U_C|\psi\rangle$ , binary bitstring  $\mathbf{s} \in \{0, 1\}^N$

- 1: Initialize:  $\text{Prob}(\mathbf{s}) = 1$ .
- 2: **for**  $n = 1, 2, \dots, N$  **do**
- 3:  $\tilde{Z}_n \leftarrow U_C^\dagger Z_n U_C$ .
- 4:  $|\psi\rangle \leftarrow \left(\frac{1}{2}I + \frac{1}{2}(-1)^{s_n} \tilde{Z}_n\right) |\psi\rangle$ .
- 5: Perform Clifford disentangling on  $U_C|\psi\rangle$ .
- 6:  $\pi(s_n|s_{1:n-1}) \leftarrow \langle \psi | \psi \rangle$ .
- 7:  $\text{Prob}(\mathbf{s}) \leftarrow \text{Prob}(\mathbf{s}) \cdot \pi(s_n|s_{1:n-1})$
- 8: **end for**

**Output:** probability for bitstring  $\mathbf{s}$ :  $\text{Prob}(\mathbf{s})$ .

---



---

### Algorithm 3 Bitstring Sampling from Clifford-MPS

---

**Input:** Clifford-MPS  $U_C|\psi\rangle$ .

- 1: Initialize: bitstring  $\mathbf{s} = ()$ ,  $\text{Prob}(\mathbf{s}) = 1$ .
- 2: **for**  $n = 1, 2, \dots, N$  **do**
- 3:  $\tilde{Z}_n \leftarrow U_C^\dagger Z_n U_C$ .
- 4:  $|\phi\rangle \leftarrow \left(\frac{1}{2}I + \frac{1}{2}\tilde{Z}_n\right) |\psi\rangle$ .
- 5: Marginal probability  $\pi(s_n = 0|s_{1:n-1}) \leftarrow \langle \phi | \phi \rangle$ .
- 6: Sample  $s_n \in \{0, 1\}$  according to probability  $\{\pi(s_n = 0|s_{1:n-1}), \pi(s_n = 1|s_{1:n-1}) = 1 - \pi(s_n = 0|s_{1:n-1})\}$
- 7:  $|\psi\rangle \leftarrow \left(\frac{1}{2}I + \frac{1}{2}(-1)^{s_n} \tilde{Z}_n\right) |\psi\rangle$ .
- 8: Perform Clifford disentangling on  $U_C|\psi\rangle$ .
- 9:  $\mathbf{s} \leftarrow (s_1, s_2, \dots, s_n)$ .
- 10:  $\text{Prob}(\mathbf{s}) \leftarrow \text{Prob}(\mathbf{s}) \cdot \pi(s_n|s_{1:n-1})$ .
- 11: **end for**

**Output:** bitstring  $\mathbf{s}$  and the corresponding probability  $\text{Prob}(\mathbf{s})$ .

---

Fig. 16(a) shows the bitstring probabilities calculated from CAMPS, are identical to the exact probabilities from MPS simulation on the same  $t$ -doped Clifford circuit. Moreover, Fig. 16(b) shows the nearly 0 (up to machine precision) KL divergence of the bitstring probabilities between the CAMPS and MPS simulations.

In Fig. 17, we examine the required MPS bond dimension during the measurement: when  $t = N/2$  (see Fig. 17(a)), the MPS bond dimension stays the same, but starts increasing after  $N/2$  qubits are measured, and eventually decreases to 1 again when all qubits are measured. Similarly, for  $t = N$ , the MPS bond dimension increases first and then decreases to 1. In Fig. 17(c), we show the maximal MPS bond dimension during the measurement grows exponentially with system size.

From the numerical simulation, we observe that the measurement on each qubit projects out one qubit from the MPS which, in the subsequent steps, typically will not be affected by  $\tilde{Z}$  from the projection operators; however,  $\tilde{Z}$  will entangle the rest unprojected qubits. For  $t < N$ , if a non-trivial Pauli term from  $\tilde{Z}_k$  hits a free qubit, a disentangling circuit can be constructed using OFD. However, once all the free qubits have been projected out by the measurement, the entanglement starts increasing among the remaining magic qubits. Generically, as indicated by Fig. 17(d), the marginal measurement on  $q \approx N - t$  qubits is efficient without increasing the MPS bond dimension. For more general cases ( $q > N - t$ ), one can measure the marginal probability on  $q$  qubits, with a computational cost exponential in  $q - \max\{0, N - t\}$ , and the measurement over all the qubits is exponentially costly in the system size.

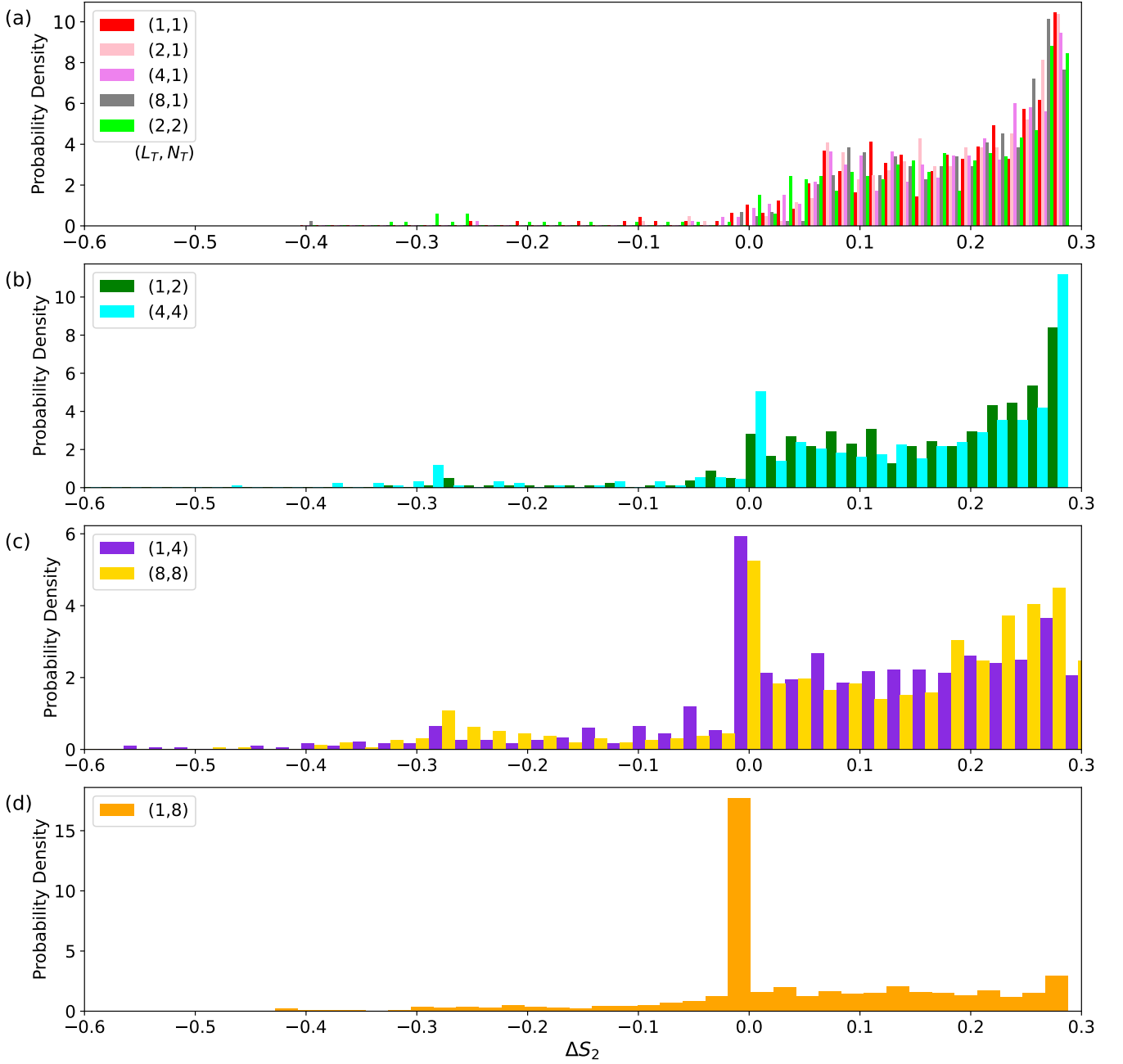


FIG. 15: In the same setting to Fig. 14, the probability densities of the MPS entropy change  $\Delta S_2$  after a  $T$ -gate is absorbed into the MPS and disentangled for various groups of  $(L_T, N_T)$ .

## B. Wavefunction Amplitude

Leveraging the ease of Pauli measurements on Clifford-MPS states, we can also obtain the (unnormalized) wavefunction amplitude for any bitstring from these states. Access to the amplitude is useful, for instance, when performing imaginary-time projection from variational states to approximate the exact ground state properties [36, 37]. The approach we present here is inspired by the scheme from quantum certification [38], but is for-

malized in a deterministic manner, owing to the special structure of CAMPS.

We begin by setting the (unnormalized) wavefunction amplitude for  $|\mathbf{s}^{[0]}\rangle = |0\rangle^{\otimes N}$  to 1. To compute the amplitude for any bitstring  $|\mathbf{s}\rangle$ , such as  $|\mathbf{s}\rangle = |0\dots 001\dots 11\rangle$ , we define a path that connects  $|\mathbf{s}^{[0]}\rangle$  and  $|\mathbf{s}\rangle$  by turning on the 1's in the following bitstring sequence, one by one:

$$\mathbf{s}^{[0]} \rightarrow \mathbf{s}^{[1]} \rightarrow \mathbf{s}^{[2]} \dots \rightarrow \mathbf{s}^{[w(\mathbf{s})-1]} \rightarrow \mathbf{s}^{[w(\mathbf{s})]} = \mathbf{s} \quad (24)$$

where  $\mathbf{s}^{[j]}$  and  $\mathbf{s}^{[j+1]}$  differ by a single bit, and  $w(\mathbf{s}) = |\mathbf{s}|$

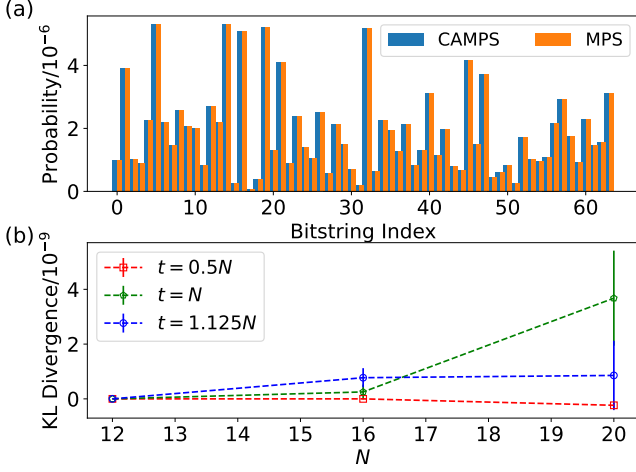


FIG. 16: Probability measurement from CAMPS: (a) Comparison with the exact probability from MPS simulation ( $N = 20, N_T = 1, t = 22$ ); (b) KL divergence of the bitstring probabilities between CAMPS and the exact MPS. Each data from (a) and (b) is averaged over 9 circuit realizations, with error bars included.

is the Hamming weight (i.e., the number of 1's) of  $\mathbf{s}$ .

Since we have defined  $\langle \mathbf{s}^{[0]} | U_C | \psi \rangle = 1$ , the calculation of  $\langle \mathbf{s} | U_C | \psi \rangle$  is completed by evaluating each ratio in the following expression:

$$\langle \mathbf{s} | U_C | \psi \rangle = \langle \mathbf{s}^{[0]} | U_C | \psi \rangle \frac{\langle \mathbf{s}^{[1]} | U_C | \psi \rangle}{\langle \mathbf{s}^{[0]} | U_C | \psi \rangle} \cdots \frac{\langle \mathbf{s} | U_C | \psi \rangle}{\langle \mathbf{s}^{[w(\mathbf{s})-1]} | U_C | \psi \rangle} \quad (25)$$

Note that  $\mathbf{s}^{[j]}$  and  $\mathbf{s}^{[j+1]}$  differ by one bit, say the  $k_j$ -th bit. We can rewrite these bitstrings as  $\mathbf{s}^{[j]} = \mathbf{s}_{1:k_j-1}^{[j]} 0 \mathbf{s}_{k_j+1:N}^{[j]} = \mathbf{s}_{N \setminus k_j}^{[j]} 0$ ,  $\mathbf{s}^{[j+1]} = \mathbf{s}_{1:k_j-1}^{[j]} 1 \mathbf{s}_{k_j+1:N}^{[j]} = \mathbf{s}_{N \setminus k_j}^{[j]} 1$ . For simplicity, we define

$$z^{[0]} = \langle \mathbf{s}_{N \setminus k_j}^{[j]} 0 | U_C | \psi \rangle, \quad z^{[1]} = \langle \mathbf{s}_{N \setminus k_j}^{[j]} 1 | U_C | \psi \rangle. \quad (26)$$

We can evaluate the probability of any bitstring using the method described in Sec. V A. Thus, we can obtain  $p_0 = |z^{[0]}|^2$ ,  $p_1 = |z^{[1]}|^2$ ,  $p_2 = |z^{[0]} + z^{[1]}|^2/2$ ,  $p_3 = |z^{[0]} - z^{[1]}|^2/2$ ,  $p_4 = |z^{[0]} + iz^{[1]}|^2/2$ , and  $p_5 = |z^{[0]} - iz^{[1]}|^2/2$ . The latter four terms are computed by appending Hadamard and phase gates to  $U_C$ , changing the eigenstates of Pauli Z operator to those of Pauli X or Y. Finally, the ratio factor in Eq. (25) is given by

$$\frac{z^{[1]}}{z^{[0]}} = \frac{p_2 - ip_4 - \frac{1}{2}(1-i)(p_0 + p_1)}{p_0}. \quad (27)$$

In Fig. 18, we present the amplitudes from a Clifford-MPS representing the state from a  $t$ -doped Clifford circuit ( $N = 12, N_T = 1, t = 2N$ ), and note that it reproduces the same results as the exact ones from the MPS simulation.

### C. Entanglement Rényi Entropy

We present an algorithm for estimating the entanglement Rényi entropy (ERE) of the full CAMPS states when the MPS represents a product state. Specifically, this algorithm generalizes the standard entropy-calculation method for stabilizer states [39] to cases where the product states include magic states, and it outperforms traditional entropy calculation methods that rely on using MPS to simulate entire states, offering a more efficient, albeit still exponential, approach for calculating the entanglement entropy of ( $t \leq N$ )-doped Clifford circuits.

We denote the Clifford-Product state with density matrix  $\rho$  as:

$$\rho = U_C |\phi\rangle \langle \phi| U_C^\dagger \quad (28)$$

and partition the  $N$ -qubit system into regions  $A$  and  $\bar{A}$  containing  $N_A$  and  $N_{\bar{A}}$  qubits, respectively ( $N_A + N_{\bar{A}} = N$ ). The density matrix for the product state can be decomposed into a product of single-qubit density matrices, i.e.,

$$\tilde{\rho} = |\phi\rangle \langle \phi| = \prod_{j=1}^N \tilde{\rho}_j \quad (29)$$

The second entanglement Rényi entropy is defined as

$$S_2 = -\ln \text{Tr}_A (\rho_A^2) \quad (30)$$

where  $\rho_A = \text{Tr}_{\bar{A}} \rho$ . Representing the density matrices in terms of Pauli strings, we write:

$$\rho = \frac{1}{2^N} \sum_{\sigma \in \mathcal{P}_N} a_\sigma \sigma \quad (31)$$

where  $a_\sigma = \text{Tr}(\sigma \rho)$ , The reduced density matrix for region  $A$  then becomes:

$$\rho_A = \frac{1}{2^{N_A}} \sum_{\sigma \in \mathcal{P}_A} a_\sigma \sigma \quad (32)$$

where  $\mathcal{P}_A$  denotes the Pauli strings restricted to region  $A$ . Thus, calculating the entanglement Rényi entropy Eq. (30) reduces to evaluating the coefficients  $a_\sigma$  for Pauli strings  $\sigma$  that have identity operators outside region  $A$ :

$$S_2 = -\ln \left( \frac{1}{2^{N_A}} \sum_{\sigma \in \mathcal{P}_A} a_\sigma^2 \right) \quad (33)$$

Although the number of terms grows exponentially with the size of region  $A$ , the computational cost can be reduced by identifying the Pauli strings with nonzero coefficients, though the exponential complexity is not guaranteed to always be removed [40]. The standard entropy-calculation method for stabilizer states [39], along with the algorithm proposed here, can be effectively interpreted as realizations of this strategy.

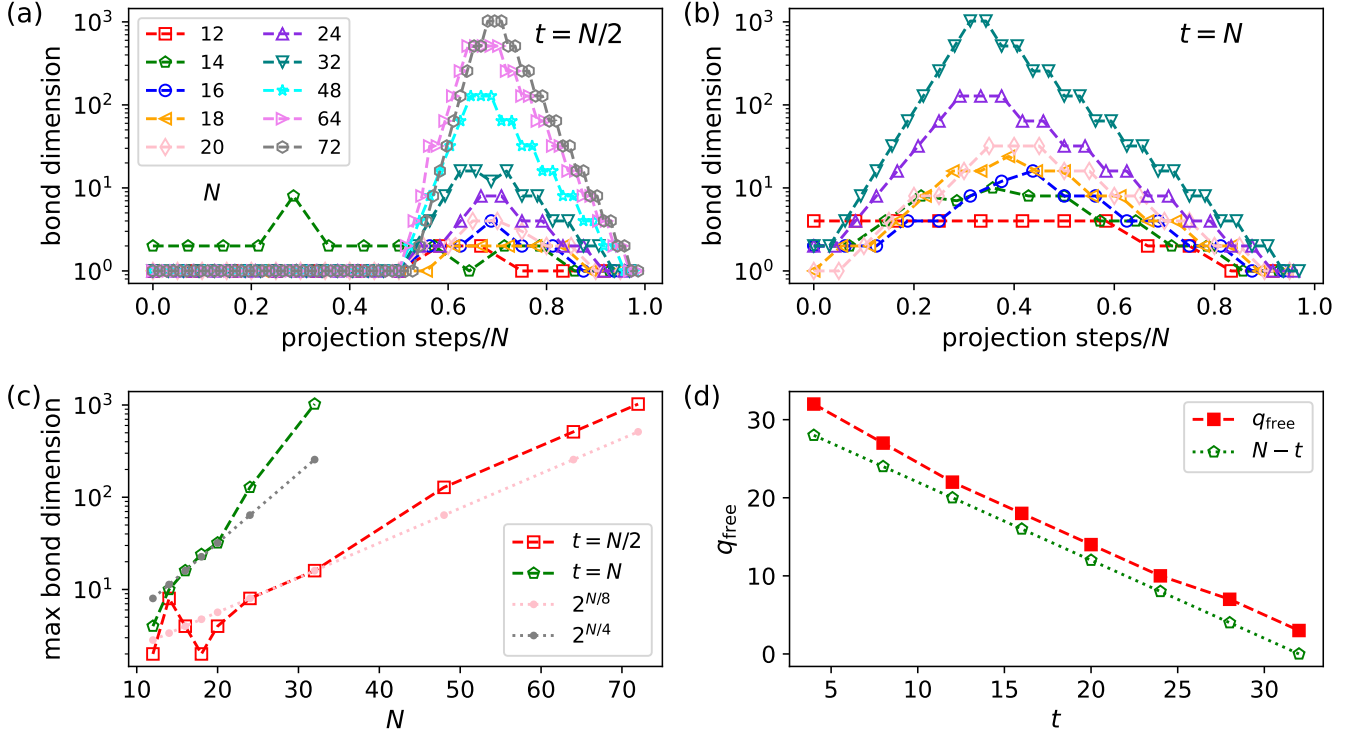


FIG. 17: Evolution of the MPS bond dimension during the probability measurement using CAMPS: (a)  $t = 0.5N$ ; (b)  $t = N$ ; (c) the maximal bond dimension as a function of system size  $N$ . Dotted lines  $2^{N/8}$  and  $2^{N/4}$  are drawn to contrast with the exponential growth from  $t = 0.5N$  and  $t = N$ , respectively. (d) The number of measured qubits for which the MPS bond dimension starts increasing during the measurement ( $q_{\text{free}}$ ) as a function of  $t$  ( $N = 32$ ,  $N_T = 1$ ); dotted line  $N - t$  is drawn for comparison.

To find the non-vanishing Pauli strings for  $\rho$ , we begin by identifying the non-vanishing generators from  $\tilde{\rho}$ . Since  $\tilde{\rho}$  is a product state, this process is efficient; we only need to examine single-qubit Pauli operators for each qubit in  $\tilde{\rho}$ . The non-vanishing generators thus originate from the  $3N$  single-qubit Pauli operators, defined as

$$\{\tilde{G}_j | \text{Tr}(\tilde{G}_j \tilde{\rho}) \neq 0, j = 1, 2, \dots, \tilde{M}\} \quad (34)$$

where the number of these generators  $\tilde{M} \leq 3N$ .

Now, let us delve into the efficiency of this step. For a stabilizer state, the action of Pauli strings maps the state back to itself with a coefficient of  $\pm 1$  or  $0$ . This gives rise to the favorable property for stabilizer states  $|\psi\rangle$ :

$$\tilde{a}_{\sigma_1 \sigma_2} = \langle \psi | \sigma_1 \sigma_2 | \psi \rangle = \langle \psi | \sigma_1 | \psi \rangle \langle \psi | \sigma_2 | \psi \rangle = \tilde{a}_{\sigma_1} \tilde{a}_{\sigma_2} \quad (35)$$

For a non-product  $\tilde{\rho}$ , where there exist qubits entangled in clusters, Eq. (35) does not hold in general. However, the product states, or states with small clusters, partially mitigate this problem: if  $\sigma_1$  and  $\sigma_2$  belongs to two unentangled regions respectively, we still have  $\tilde{a}_{\sigma_1 \sigma_2} = \tilde{a}_{\sigma_1} \tilde{a}_{\sigma_2}$ . Consequently, it suffices to check Pauli strings within each cluster, with complexity growing only exponentially with cluster size, i.e.,  $\sup \tilde{M} = \sum_R 3^{|R|}$ , where  $|R|$  is the qubit number in each cluster  $R$  ( $\sum_R |R| = N$ ).

For product states, each cluster size  $|R|$  is always 1, yielding  $\sup \tilde{M} = 3N$ .

For clusters of size 1 (i.e., single qubit unentangled from the rest), we need to check all the three Pauli operators on that qubit, because for magic qubits created by the  $T$  gates, two out of the three Pauli operators can have nonzero coefficients, while for stabilizer states, only one non-vanishing Pauli operator exists for each qubit.

After identifying the generator set  $\{\tilde{G}_j\}_{j=1}^{\tilde{M}}$  with non-zero coefficients from  $\tilde{\rho}$ , we map these generators to the Pauli strings for  $\rho$  and select the subset needed to generate the Pauli strings in Eq. (32). The mapping is achieved by

$$G_j = U_C \tilde{G}_j U_C^\dagger \quad (36)$$

To isolate the subset of generators that correspond to  $\sigma \in \mathcal{P}_A$ , we use Gaussian elimination to remove, as many as possible, the non-identity operators in region  $\bar{A}$ , yielding:

$$\{Q_j \subseteq \langle \{G_j\}_{j=1}^{\tilde{M}} \rangle | Q_j \in \mathcal{P}_A \otimes I^{\otimes N_A}, j = 1, 2, \dots, M\} \quad (37)$$

where  $M \leq \tilde{M}$  represents the number of generators identified through Gaussian elimination. During this process,

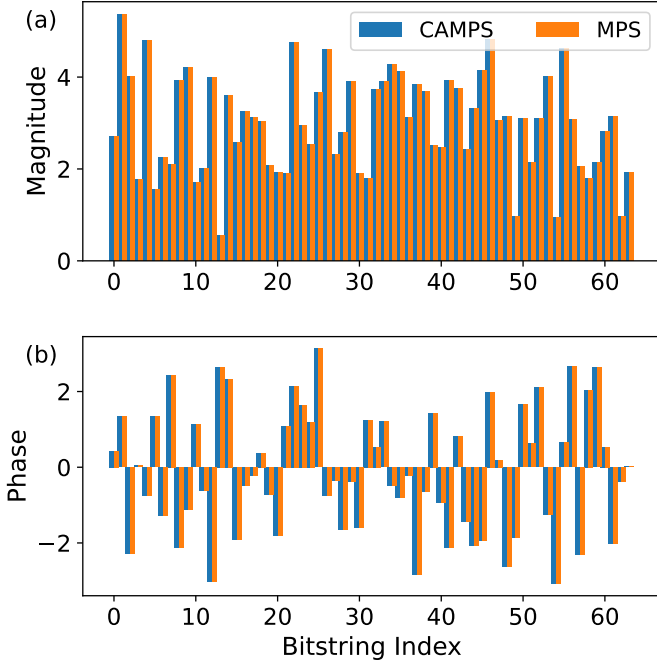


FIG. 18: (a) The magnitude and (b) the phase of the unnormalized wave function amplitude from CAMPS ( $N = 12, N_T = 1, t = 2N$ ). Exact results obtained from MPS simulation are included for comparison.

we track the decomposition of each  $Q$ 's in terms of  $G$ 's:

$$Q_j = \prod_{k=1}^{\tilde{M}} G_k^{K_k^j} \quad (38)$$

where  $K_k^j \in \{0, 1\}$  indicates the presence of  $G_k$  in the composition of  $Q_j$ . Consequently, we find

$$\begin{aligned} a_{Q_j} &= \text{Tr}(Q_j \rho) = \text{Tr}\left(\prod_{k=1}^{\tilde{M}} G_k^{K_k^j} \rho\right) \\ &= \text{Tr}\left(\prod_{k=1}^{\tilde{M}} G_k^{K_k^j} U_C \tilde{\rho} U_C^\dagger\right) = \text{Tr}\left(U_C^\dagger \prod_{k=1}^{\tilde{M}} G_k^{K_k^j} U_C \tilde{\rho}\right) \\ &= \text{Tr}\left(\prod_{k=1}^{\tilde{M}} \tilde{G}_k^{K_k^j} \tilde{\rho}\right) \end{aligned} \quad (39)$$

This expression enables the calculation of the coefficients  $a_{Q_j}$  based on the transformations applied to the generators  $\{\tilde{G}\}$ .

As we have noted, even for Clifford-Product states, Eq. (35) does not hold if, for instance,  $\sigma_1$  and  $\sigma_2$  are Pauli operators on the same magic qubit. Thus, the set  $\{Q_j\}_{j=1}^M$  obtained from Gaussian elimination may still produce Pauli strings with zero coefficients. In contrast, for stabilizer states, Eq. (35) ensures that  $\{Q_j\}_{j=1}^M$  will

only generate Pauli strings with non-zero coefficients, which are already known to be  $\pm 1$ ; thus for stabilizer states, there are  $2^M$  Pauli strings in region  $A$  with non-vanishing coefficients of  $\pm 1$ , yielding  $S_2 = (N_A - M) \ln 2$  according to Eq. (33).

This process of identifying the non-zero Pauli generators essentially mirrors the standard method for calculating entropy in stabilizer states [39]. We now introduce two approaches to finalize the computation of entanglement entropy with the set of non-zero Pauli generators.

The first approach involves enumerating all Pauli strings generated by  $\{Q_j\}_{j=1}^M$  and calculating the coefficients for each. While straightforward, this method has exponential complexity,  $\mathcal{O}(2^M)$ , making it practical only for modest values of  $M$  regardless of the system size.

The second approach aims to represent these coefficients using a new MPS, from which Eq. 33 can be derived as the norm of this new MPS. This approach, while still potentially exponential, allows a series of systematically improvable approximations associated with truncating the MPS bond-dimension. We begin by rewriting the reduced density matrix  $\rho_A$  in terms of  $\{Q_j\}_{j=1}^M$ :

$$\rho_A = \frac{1}{2^{N_A}} (I + a_{Q_1} Q_1) \circ (I + a_{Q_2} Q_2) \circ \cdots \circ (I + a_{Q_M} Q_M) \quad (40)$$

where  $\circ$  is defined as:

$$\begin{aligned} (a_{\sigma_1} \sigma_1) \circ (a_{\sigma_2} \sigma_2) &= a_{\sigma_1 \sigma_2} \sigma_1 \sigma_2 \\ (a_{\sigma_1} \sigma_1 + a_{\sigma_2} \sigma_2) \circ (a_{\sigma_3} \sigma_3) &= a_{\sigma_1 \sigma_3} \sigma_1 \sigma_3 + a_{\sigma_2 \sigma_3} \sigma_2 \sigma_3 \\ (I) \circ (a_{\sigma} \sigma) &= a_{\sigma} \sigma \\ \circ_{k=1}^K (a_{\sigma_k} \sigma_k) &= (a_{\sigma_1} \sigma_1) \circ (a_{\sigma_2} \sigma_2) \circ \cdots \circ (a_{\sigma_K} \sigma_K) \end{aligned} \quad (41)$$

Note that even if  $a_{Q_j} = 0$  for one factor in Eq. (40), combining it with others may still yield non-zero Pauli strings. According to Eq. (39), we find

$$a_{Q_j} Q_j = \circ_{k=1}^{\tilde{M}} (\tilde{a}_{\tilde{G}_k} \tilde{G}_k)^{K_k^j} \quad (42)$$

Now, we introduce a new type of quantum state as

$$|\rho_A\rangle = \frac{1}{2^{N_A/2}} \prod_{j=1}^M \left(1 + \prod_{k=1}^{\tilde{M}} (c_k^\dagger)^{K_k^j}\right) |0\rangle \quad (43)$$

where the creation operators  $\{c_k^\dagger\}_{k=1}^{\tilde{M}}$  aligns with  $\{\tilde{a}_{\tilde{G}_k} \tilde{G}_k\}_{k=1}^{\tilde{M}}$  via:

$$\tilde{a}_{\tilde{G}_k} \tilde{G}_k \iff c_k^\dagger |0\rangle = \tilde{a}_{\tilde{G}_k} |1\rangle \quad (44)$$

$$\circ (\tilde{a}_{\tilde{G}_k} \tilde{G}_k)^2 = I^N \iff c_k^\dagger |1\rangle = \frac{1}{\tilde{a}_{\tilde{G}_k}} |0\rangle \quad (45)$$

$$(\tilde{a}_{\tilde{G}_{k_1}} \tilde{G}_{k_1}) \circ (\tilde{a}_{\tilde{G}_{k_2}} \tilde{G}_{k_2}) = 0 \iff c_{k_1}^\dagger c_{k_2}^\dagger |00\rangle = 0 \quad (46)$$

The first two properties define a matrix product operator for  $c_k^\dagger$ :

$$\mathbb{O}_k = \begin{pmatrix} 0 & \frac{1}{\tilde{a}_{\tilde{G}_k}} \\ \tilde{a}_{\tilde{G}_k} & 0 \end{pmatrix} \quad (47)$$

Since the signs of the coefficients do not impact Rényi entropy, we define the commutation relation as  $c_k^\dagger c_j^\dagger = c_j^\dagger c_k^\dagger$ ,  $\forall j, k$ . Expanding  $|\rho_A\rangle$  in basis states, such as  $|0100\dots 0\rangle$ , gives the  $a_\sigma$  coefficients from Eq. (32). The square norm,

$$\langle \rho_A | \rho_A \rangle = \sum_{\sigma} a_{\sigma}^2 \quad (48)$$

yields the second Rényi entropy as per Eq. (33).

Representing  $|\rho_A\rangle$  as an MPS follows the standard MPO-MPS contraction process [20]. Since the MPO involves long-range creation of quantum states, the resulting MPS can require a large bond dimension during this process. We can optimize the sequence of the creation operators from Eq. (43), such that the bond dimension in the intermediate steps does not increase severely. For instance, the property Eq. (46) is likely to decrease the bond dimension, so we prefer to implement them as early as possible. To this end, we use Gaussian elimination to move the Pauli strings satisfying Eq. (46) to the first few MPO-MPS contraction steps. Besides, the qubit positions corresponding to the creation of  $c_k^\dagger$  or  $\tilde{G}_k$  are adjustable, so that the long-range correlation incurred in MPS can be further reduced. We expect this direction of optimization can be further explored in future work. Noticeably, if we use this second approach to calculate the entropy for stabilizer states, we have  $\mathbb{O}_k = X$ , then, even if the number of  $Q$ 's can be large,  $|\rho_A\rangle$  forms a stabilizer state, allowing efficient representation through the Clifford-MPS and Clifford disentangling algorithm. We refer to the two methods introduced here as the Pauli Coefficient Enumeration (PCE) and Pauli Coefficient Matrix Product State (PCMPS) methods.

In Fig. 19, we show the Rényi entropy calculated using PCMPS method. First, in Fig. 19(a), we apply PCMPS to a Clifford circuit ( $N = 128$ ) and demonstrate that it reproduces the exact results. Moreover, the bond dimension of PCMPS remains as 1, as shown in Fig. 19(b), indicating the application of PCMPS to Clifford circuits is polynomially efficient. Next, we apply it to  $t$ -doped Clifford circuits up to 64 qubits: as shown in Fig. 19(c), it reproduces the exact results in small systems, and outperforms the results from MPS simulation with comparable bond dimensions. Fig. 19(d) shows the bond dimension from PCMPS during the calculation of entropy: for  $N = 48$  and  $N = 64$ , bond truncation is involved.

## VI. CONCLUSIONS

In this work, we have investigated the classical simulability of  $t$ -doped Clifford circuits using CAMPS as an efficient representation for the underlying quantum states.

Contrary to the impressions that the classical resources have to grow exponentially with  $t$  – the number of non-Clifford gates (e.g.,  $T$ -gates) – we show that the disentangling procedure of CAMPS can avoid increasing the entanglement on (the correct) Pauli strings coming from  $N$   $T$ -gates making those  $T$ -gates free to simulate. Under a simplified model that these Pauli strings are random in the light-cone induced by the  $T$ -gates, we find that the  $T$ -gates which are deep enough to induce windows of logarithmic or poly-logarithmic size will typically be free  $T$ -gates. Because in one-dimension, it is efficient to simulate out to this depth (either in polynomial or quasi-polynomial time), this would suggest that circuits with  $t \leq N$  are classically simulatable in one-dimension. In higher dimensions, this classical simulatability would likely exist for  $t$ -doped circuits where the  $T$ -gates are sufficiently deep.

To represent the quantum state from a  $t$ -doped Clifford circuit using CAMPS, the stabilizer and the non-stabilizer components are separated apart and represented concisely with a stabilizer tableau ( $U_C$ ) and an MPS ( $|\psi\rangle$ ), respectively. In particular, when encountering a  $T$ -gate from the circuit, we first commute it through the Clifford layers to the front of MPS; this gives us an operator to act on the MPS, i.e.,  $\tilde{T} = U_C^\dagger T U_C = \alpha I + \beta \tilde{Z}$  and thereby  $|\psi\rangle \leftarrow \tilde{T}|\psi\rangle$ . However, one can introduce a new set of Clifford gates to reduce the entanglement of  $\tilde{T}|\psi\rangle$ . We developed a novel algorithm, OFD, which uses (long-range) control-Pauli gates to perform this disentangling for a set of specific  $N$   $T$ -gates. We then show that the heuristic optimization of OBD typically matches this.

The OFD algorithm works by picking up a non-magic qubit flipped by the non-trivial Pauli term from  $\tilde{Z}$  and using it as the control qubit to unflip all the other flipped qubits using control-Pauli gates. Compared to OBD, OFD reveals the condition (i.e., the presence of control qubits) for CAMPS being able to represent the ( $t \lesssim N$ )-doped Clifford circuit efficiently, with the MPS component typically representing a product state. This condition is determined by the Pauli string set commuted from the  $T$ -gates. We provide analytic and numerical arguments describing when all but a logarithmic or logarithmic squared number of free Pauli strings – enabling the application of OFD – show up in the first  $N$   $T$ -gates. We examine our analysis with extensive numerical experiments, including random  $t$ -doped Clifford circuits on one and two spatial dimensions, as well as the circuits with constraints on the gate distributions. Furthermore, we have extended the numerical experiments beyond  $t \leq N$ , and observed the collapse the MPS entanglement across various values of  $T$ -gate number per layer and the system size, suggesting a non-trivial dependence of the MPS entanglement dynamics on the structure of quantum circuits.

Finally, we introduce algorithms for the calculation of (1) the probability (and the sampling) of bitstring from the CAMPS, (2) the wave function amplitude, and (3)

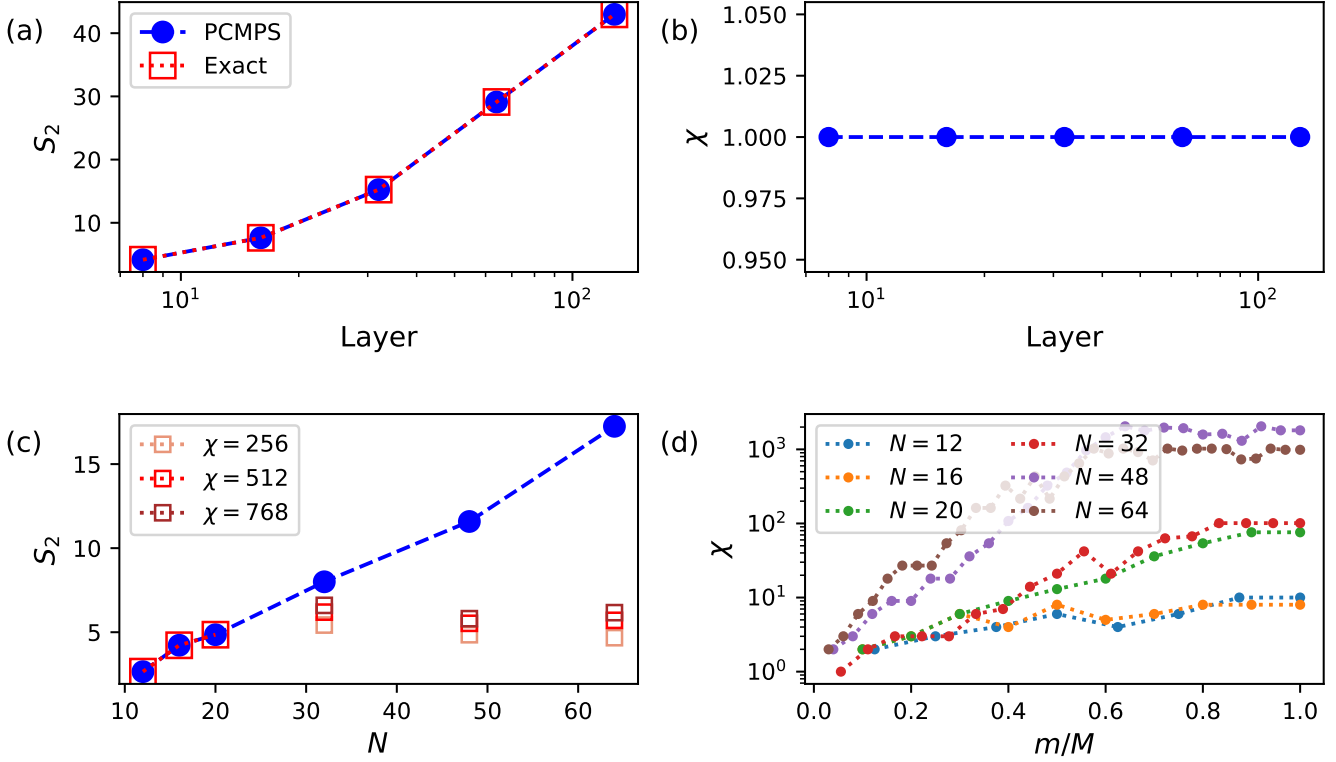


FIG. 19: (a) Second Rényi entropy of CAMPS on a Clifford circuit ( $N = 128$ , brick-wall circuit architecture), with exact results from the standard Clifford entropy algorithm included for comparison, and (b) the bond dimension of PCMPS as a function of circuit layer; (c) Second Rényi entropy of CAMPS on  $t$ -doped Clifford circuits ( $N_T = 1, t = N/2$ ) as a function of qubit number, with the results from MPS simulation included for comparison (for  $N \geq 32$ ,  $\chi_{\max}$  for MPS is set to as  $\{256, 512, 768\}$ ), and (d) the bond dimension of PCMPS during the simulation process.

the entanglement Rényi entropy of CAMPS. The algorithms for (1) and (2) are similar to that of converting from  $t$ -doped Clifford circuits to the representation of CAMPS, and differ by replacing the non-Clifford gates with projection operators for measurement. While the final state after measuring all the qubits is a computational basis product state, the intermediate states during the measurement are observed to display an exponential growth on the MPS bond dimension once the measured qubit number  $q > N - t$ . For task (3), we develop an algorithm which constructs an MPS to represent the non-zero Pauli coefficients of CAMPS, and the entanglement Rényi entropy is then calculated from the norm of MPS representation. The complexity of this algorithm depends on the number of non-vanishing Pauli generators instead of the system size. We numerically show that it has polynomial cost on Clifford circuits, while on  $t$ -doped Clifford circuits, encounters exponential cost, though, is able to outperform the traditional tensor-network simulation method.

While this work establishes a computational framework for the simulation of  $t$ -doped Clifford circuits, we expect it also contributes to the growing interest on the interplay between quantum entanglement and quantum magic and their roles in the boundary between classical simulability and quantum advantage, as well as inspires new efficient algorithms for the simulation of quantum systems [29, 30, 40–43].

## ACKNOWLEDGMENTS

We would like to thank X. Feng for insightful discussions. This work made use of the Illinois Campus Cluster, a computing resource that is operated by the Illinois Campus Cluster Program (ICCP) in conjunction with the National Center for Supercomputing Applications (NCSA) and which is supported by funds from the University of Illinois at Urbana-Champaign.

[1] R. P. Feynman, Simulating physics with computers, in *Feynman and computation* (cRc Press, 2018) pp. 133–

- [2] D. Aharonov, Quantum to classical phase transition in noisy quantum computers, *Phys. Rev. A* **62**, 062311 (2000).
- [3] D. Aharonov, X. Gao, Z. Landau, Y. Liu, and U. Vazirani, A polynomial-time classical algorithm for noisy random circuit sampling, in *Proceedings of the 55th Annual ACM Symposium on Theory of Computing* (2023) pp. 945–957.
- [4] A. Angrisani, A. Schmidhuber, M. S. Rudolph, M. Cerezo, Z. Holmes, and H.-Y. Huang, Classically estimating observables of noiseless quantum circuits, arXiv preprint arXiv:2409.01706 (2024).
- [5] K. Kechedzhi, S. V. Isakov, S. Mandrà, B. Villalonga, X. Mi, S. Boixo, and V. Smelyanskiy, Effective quantum volume, fidelity and computational cost of noisy quantum processing experiments, *Future Generation Computer Systems* **153**, 431 (2024).
- [6] F. Pan, K. Chen, and P. Zhang, Solving the sampling problem of the sycamore quantum circuits, *Phys. Rev. Lett.* **129**, 090502 (2022).
- [7] R. Jozsa and A. Miyake, Matchgates and classical simulation of quantum circuits, *Proceedings of the Royal Society A: Mathematical, Physical and Engineering Sciences* **464**, 3089 (2008).
- [8] S. Aaronson and D. Gottesman, Improved simulation of stabilizer circuits, *Phys. Rev. A* **70**, 052328 (2004).
- [9] D. Gottesman, *The heisenberg representation of quantum computers* (1998), arXiv:quant-ph/9807006 [quant-ph].
- [10] J. C. Napp, R. L. La Placa, A. M. Dalzell, F. G. S. L. Brandão, and A. W. Harrow, Efficient classical simulation of random shallow 2d quantum circuits, *Phys. Rev. X* **12**, 021021 (2022).
- [11] G. Vidal, Efficient classical simulation of slightly entangled quantum computations, *Phys. Rev. Lett.* **91**, 147902 (2003).
- [12] G. Vidal, Efficient simulation of one-dimensional quantum many-body systems, *Phys. Rev. Lett.* **93**, 040502 (2004).
- [13] F. Pan and P. Zhang, Simulation of quantum circuits using the big-batch tensor network method, *Phys. Rev. Lett.* **128**, 030501 (2022).
- [14] B. Villalonga, M. Y. Niu, L. Li, H. Neven, J. C. Platt, V. N. Smelyanskiy, and S. Boixo, Efficient approximation of experimental gaussian boson sampling, arXiv preprint arXiv:2109.11525 (2021).
- [15] T. Begušić, J. Gray, and G. K.-L. Chan, Fast and converged classical simulations of evidence for the utility of quantum computing before fault tolerance, *Science Advances* **10**, eadk4321 (2024).
- [16] J. Tindall, M. Fishman, E. M. Stoudenmire, and D. Sels, Efficient tensor network simulation of ibm’s eagle kicked ising experiment, *PRX Quantum* **5**, 010308 (2024).
- [17] M. A. Nielsen and I. L. Chuang, *Quantum computation and quantum information*, Vol. 2 (Cambridge university press Cambridge, 2001).
- [18] B. Zeng, X. Chen, D.-L. Zhou, X.-G. Wen, *et al.*, *Quantum information meets quantum matter* (Springer, 2019).
- [19] F. Pollmann, A. M. Turner, E. Berg, and M. Oshikawa, Entanglement spectrum of a topological phase in one dimension, *Phys. Rev. B* **81**, 064439 (2010).
- [20] R. Orús, A practical introduction to tensor networks: Matrix product states and projected entangled pair states, *Annals of Physics* **349**, 117 (2014).
- [21] Z.-C. Gu, M. Levin, B. Swingle, and X.-G. Wen, Tensor-product representations for string-net condensed states, *Phys. Rev. B* **79**, 085118 (2009).
- [22] A. Y. Kitaev, Fault-tolerant quantum computation by anyons, *Annals of physics* **303**, 2 (2003).
- [23] S. Bravyi, D. Browne, P. Calpin, E. Campbell, D. Gosset, and M. Howard, Simulation of quantum circuits by low-rank stabilizer decompositions, *Quantum* **3**, 181 (2019).
- [24] A. Kissinger and J. van de Wetering, Simulating quantum circuits with zx-calculus reduced stabiliser decompositions, *Quantum Science and Technology* **7**, 044001 (2022).
- [25] T. Begušić, K. Hejazi, and G. K.-L. Chan, *Simulating quantum circuit expectation values by clifford perturbation theory* (2023), arXiv:2306.04797 [quant-ph].
- [26] H. Pashayan, O. Reardon-Smith, K. Korzekwa, and S. D. Bartlett, Fast estimation of outcome probabilities for quantum circuits, *PRX Quantum* **3**, 020361 (2022).
- [27] G. Lami, T. Haug, and J. D. Nardis, *Quantum state designs with clifford enhanced matrix product states* (2024), arXiv:2404.18751 [quant-ph].
- [28] X. Qian, J. Huang, and M. Qin, Augmenting density matrix renormalization group with clifford circuits, *Phys. Rev. Lett.* **133**, 190402 (2024).
- [29] J. Huang, X. Qian, and M. Qin, *Non-stabilizerness entanglement entropy: a measure of hardness in the classical simulation of quantum many-body systems* (2024), arXiv:2409.16895 [quant-ph].
- [30] G. E. Fux, B. Béri, R. Fazio, and E. Tirrito, *Disentangling unitary dynamics with classically simulable quantum circuits* (2024), arXiv:2410.09001 [quant-ph].
- [31] A. F. Mello, A. Santini, G. Lami, J. D. Nardis, and M. Collura, *Clifford dressed time-dependent variational principle* (2024), arXiv:2407.01692 [quant-ph].
- [32] X. Qian, J. Huang, and M. Qin, *Clifford circuits augmented time-dependent variational principle* (2024), arXiv:2407.03202 [cond-mat.str-el].
- [33] C. Gidney, Stim: a fast stabilizer circuit simulator, *Quantum* **5**, 497 (2021).
- [34] Y. Zhou, E. M. Stoudenmire, and X. Waintal, What limits the simulation of quantum computers?, *Phys. Rev. X* **10**, 041038 (2020).
- [35] T. Ayril, T. Louvet, Y. Zhou, C. Lambert, E. M. Stoudenmire, and X. Waintal, Density-matrix renormalization group algorithm for simulating quantum circuits with a finite fidelity, *PRX Quantum* **4**, 020304 (2023).
- [36] D. M. Ceperley and B. J. Alder, Ground state of the electron gas by a stochastic method, *Phys. Rev. Lett.* **45**, 566 (1980).
- [37] R. M. Martin, L. Reining, and D. M. Ceperley, *Interacting electrons* (Cambridge University Press, 2016).
- [38] H.-Y. Huang, J. Preskill, and M. Soleimanifar, *Certifying almost all quantum states with few single-qubit measurements* (2024), arXiv:2404.07281 [quant-ph].
- [39] D. Fattal, T. S. Cubitt, Y. Yamamoto, S. Bravyi, and I. L. Chuang, *Entanglement in the stabilizer formalism* (2004), arXiv:quant-ph/0406168 [quant-ph].
- [40] A. Gu, S. F. E. Oliviero, and L. Leone, *Magic-induced computational separation in entanglement theory* (2024), arXiv:2403.19610 [quant-ph].
- [41] M. Bejan, C. McLauchlan, and B. Béri, Dynamical magic transitions in monitored clifford+*t* circuits, *PRX Quantum* **5**, 030332 (2024).
- [42] Y. Zhang and Y. Zhang, *Classical simulability of*

quantum circuits with shallow magic depth (2024), arXiv:2409.13809 [quant-ph].

- [43] Z. Liu and B. K. Clark, Non-equilibrium quantum monte carlo algorithm for stabilizer renyi entropy in spin systems (2024), arXiv:2405.19577 [quant-ph].
- [44] G. Lami and M. Collura, Unveiling the stabilizer group of a matrix product state, *Phys. Rev. Lett.* **133**, 010602 (2024).

## Appendix A: Concepts and Notations

In this section we introduce the basic concepts and notations used throughout this work. We denote the identity and Pauli operators as

$$\begin{aligned} I &= \begin{pmatrix} 1 & 0 \\ 1 & 0 \end{pmatrix}, & X &= \begin{pmatrix} 0 & 1 \\ 1 & 0 \end{pmatrix}, \\ Y &= \begin{pmatrix} 0 & -i \\ i & 0 \end{pmatrix}, & Z &= \begin{pmatrix} 1 & 0 \\ 0 & -1 \end{pmatrix}. \end{aligned} \quad (\text{A1})$$

For a quantum system composed of  $N$  qubits, we represent Pauli strings as the tensor product of Pauli and identity operators across the system, denoted by  $\boldsymbol{\sigma}$ , i.e.,  $\boldsymbol{\sigma} = \otimes_{j=1}^N \sigma_j = \sigma_1 \sigma_2 \cdots \sigma_N$ , where  $\sigma_j \in \{I, X, Y, Z\}$ . A substring, for example, from qubit 1 to qubit  $n$ , is denoted as  $\boldsymbol{\sigma}_{1:n} \equiv \sigma_1 \sigma_2 \cdots \sigma_n$ . The set of all  $N$ -qubit Pauli strings is called the Pauli group, denoted as  $\mathcal{P}_N$ .

Clifford circuits are composed of Clifford gates, a class of unitary operators that can be generated by the Hadamard, phase, and CNOT (control-X) gates:

$$H = \frac{1}{\sqrt{2}} \begin{pmatrix} 1 & 1 \\ 1 & -1 \end{pmatrix}, \quad S = \begin{pmatrix} 1 & 0 \\ 0 & i \end{pmatrix}, \quad (\text{A2})$$

$$CX = \begin{pmatrix} 1 & 0 & 0 & 0 \\ 0 & 1 & 0 & 0 \\ 0 & 0 & 0 & 1 \\ 0 & 0 & 1 & 0 \end{pmatrix}. \quad (\text{A3})$$

An important property of the Clifford group is that the element  $U_C$  of it leaves the Pauli group invariant under conjugation: for all  $P \in \mathcal{P}_N$ ,  $U_C P U_C^\dagger \in \mathcal{P}_N$ .

In addition, we list the two-qubit Clifford gates useful in this work. The basis states in the matrix format  $O_{j,k}$  are on the order of  $|s_j s_k\rangle = |00\rangle, |01\rangle, |10\rangle, |11\rangle$ .

$$\text{SWAP} = \begin{pmatrix} 1 & 0 & 0 & 0 \\ 0 & 0 & 1 & 0 \\ 0 & 1 & 0 & 0 \\ 0 & 0 & 0 & 1 \end{pmatrix} \quad (\text{A4})$$

$$\text{XC} = \begin{pmatrix} 1 & 0 & 0 & 0 \\ 0 & 0 & 0 & 1 \\ 0 & 0 & 1 & 0 \\ 0 & 1 & 0 & 0 \end{pmatrix} \quad (\text{A5})$$

$$\text{CZ} = \begin{pmatrix} 1 & 0 & 0 & 0 \\ 0 & 1 & 0 & 0 \\ 0 & 0 & 1 & 0 \\ 0 & 0 & 0 & -1 \end{pmatrix}, \quad \text{ZC} = \begin{pmatrix} 1 & 0 & 0 & 0 \\ 0 & 1 & 0 & 0 \\ 0 & 0 & 1 & 0 \\ 0 & 0 & 0 & -1 \end{pmatrix} \quad (\text{A6})$$

$$\text{CY} = \begin{pmatrix} 1 & 0 & 0 & 0 \\ 0 & 1 & 0 & 0 \\ 0 & 0 & 0 & -i \\ 0 & 0 & i & 0 \end{pmatrix}, \quad \text{YC} = \begin{pmatrix} 1 & 0 & 0 & 0 \\ 0 & 0 & 0 & -i \\ 0 & 0 & 1 & 0 \\ 0 & i & 0 & 0 \end{pmatrix} \quad (\text{A7})$$

Note that here we have introduced the notations such as XC for the control-Pauli gates whose control qubit is the second qubit and target qubit is the first qubit.

The non-Clifford gate considered in this work is the  $T$ -gate:

$$T = \begin{pmatrix} 1 & 0 \\ 0 & e^{i\pi/4} \end{pmatrix}. \quad (\text{A8})$$

Notably, adding  $T$ -gates to Clifford circuits enables universal quantum computation.

Throughout this paper, we denote vectors with bold lowercase letters (e.g.,  $\mathbf{a}$ ,  $\mathbf{g}$ ), and matrices with bold uppercase letters (e.g.,  $\mathbf{B}$ ,  $\mathbf{C}$ ), with elements represented by regular letters with indices (e.g.,  $a_j$ ,  $B_{jk}$ ). Meanwhile, for a Pauli string  $P$ , we can express it as  $P = i^{\sum_n x_n z_n} \prod_{n=1}^N X_n^{x_n} Z_n^{z_n}$ , where  $X_n$  ( $Z_n$ ) are Pauli  $Z$  ( $X$ ) operators on the  $n$ -th qubit, and the elements of vector  $\mathbf{x}$  ( $\mathbf{z}$ )  $\in \{0, 1\}^N$  indicate the presence of  $X_n$  ( $Z_n$ ).

## Appendix B: Stabilizer Tableau for Clifford Circuits

The most common approach to representing a Clifford circuit involves tracking the set of stabilizer generators that leave the output state of the circuit invariant [8, 9]. Specifically, for an  $N$ -qubit Clifford circuit  $U_C$  acting on the computational basis state  $|0\rangle^{\otimes N}$ , the resulting state  $|\psi\rangle = U_C|0\rangle^{\otimes N}$  is stabilized by any operator  $C$  generated by the stabilizer generators  $\{g_j\}_{j=1}^N$ , meaning  $C|\psi\rangle = |\psi\rangle$ . These generators can be expressed as  $g_j = U_C Z_j U_C^\dagger$ . However, for our purposes, it is not sufficient to track only  $U_C Z_j U_C^\dagger$ , since the Clifford circuit acts on arbitrary initial states, such as MPS, which are generally not stabilized by a Pauli  $Z$  operator. Thus, additional information about the Clifford circuit – specifically, the transformations on the Pauli  $X$  operator – is necessary to enable efficient simulation. To address this need, we introduce another definition of the stabilizer tableau used throughout this work for representing the Clifford circuit.

**Definition 1** (*Stabilizer tableau for Clifford circuits*) Let  $U_C$  be an  $N$ -qubit Clifford circuit. The corresponding

tableau is defined by the action of  $U_C$  on the Pauli operators at each site  $n$ :

$$\begin{aligned} U_C^\dagger X_n U_C &= i^{g_n} \prod_{k=1}^N X_k^{D_{nk}} Z_k^{F_{nk}} \\ U_C^\dagger Z_n U_C &= i^{a_n} \prod_{k=1}^N X_k^{B_{nk}} Z_k^{C_{nk}} \end{aligned} \quad (\text{B1})$$

where  $g_n, a_n \in \{0, 1, 2, 3\}$  and  $D_{nk}, F_{nk}, B_{nk}, C_{nk} \in \{0, 1\}$ . The tableau is thus constructed as a set of vectors and matrices:  $\{\mathbf{g}, \mathbf{a}, \mathbf{D}, \mathbf{F}, \mathbf{B}, \mathbf{C}\}$ .

Similar to the phase-sensitive stabilizer tableau introduced in Ref. [23], Definition 1 focuses solely on the Clifford operators themselves (allowing for applicability to arbitrary initial states) and also tracks phase factors. This approach (Definition 1), however, formalizes the representation in a simpler manner, without the need to classify Clifford gates into different types and treat them separately as done in Ref. [23].

With Definition 1, we can commute any Pauli string  $P$  through the Clifford circuit, obtaining the resulting twisted Pauli string as  $P' = U_C^\dagger P U_C$  using the following algorithm:

---

**Algorithm 4** Pauli string commuting algorithm

---

**Input:** Pauli string  $P = i^{\sum_n x_n z_n} \prod_{n=1}^N X_n^{x_n} Z_n^{z_n}$ , stabilizer tableau for the Clifford circuit  $\mathbf{g}, \mathbf{a}, \mathbf{D}, \mathbf{F}, \mathbf{B}, \mathbf{C}$ .

- 1: Initialize:  $\mathbf{X} = \mathbf{0}_{2N \times N}$ ,  $\mathbf{Z} = \mathbf{0}_{2N \times N}$ ,  $s = \sum_{n=1}^N x_n z_n$ .
- 2: **for**  $n = 1, 2, \dots, N$  **do**
- 3:   **if**  $x_n = 1$  **then**
- 4:      $\mathbf{X}[2n] \leftarrow \mathbf{D}[n]$       $\triangleright \mathbf{X}[2n] = (2n)$ -th row of  $\mathbf{X}$
- 5:      $\mathbf{Z}[2n] \leftarrow \mathbf{F}[n]$
- 6:      $s \leftarrow s + g_n$ .
- 7:   **end if**
- 8:   **if**  $z_n = 1$  **then**
- 9:      $\mathbf{X}[2n+1] \leftarrow \mathbf{B}[n]$
- 10:     $\mathbf{Z}[2n+1] \leftarrow \mathbf{C}[n]$
- 11:     $s \leftarrow s + a_n$ .
- 12:   **end if**
- 13: **end for**
- 14:  $x'_n \leftarrow \sum_{k=1}^{2N} X_{kn}$ ;  $z'_n \leftarrow \sum_{k=1}^{2N} Z_{kn}$ .
- 15:  $\mathbf{Z}^c =$  cumulative sum of  $\mathbf{Z}$  along the rows.
- 16:  $s \leftarrow s + 2 \sum_{n=1}^N \sum_{k=1}^{2N-1} Z_{kn} X_{k+1,n}$ .

**Output:** The Pauli string after commuting through the Clifford circuit  $P' = i^s \prod_{n=1}^N X_n^{x'_n} Z_n^{z'_n}$ .

---

Here we provide justification for Algorithm 4. By writing Pauli string as  $P = i^{\sum_n x_n z_n} \prod_{n=1}^N X_n^{x_n} Z_n^{z_n}$ , where

$x_n, z_n \in \{0, 1\}$ , and using Definition 1, we have

$$\begin{aligned} P' &= U_C^\dagger P U_C = i^{\mathbf{x} \cdot \mathbf{z}} \prod_{n=1}^N (U_C^\dagger X_n U_C)^{x_n} (U_C^\dagger Z_n U_C)^{z_n} \\ &= i^{\mathbf{x} \cdot \mathbf{z} + \mathbf{x} \cdot \mathbf{g} + \mathbf{z} \cdot \mathbf{a}} \prod_{n=1}^N \left( \prod_k X_k^{D_{nk}} Z_k^{F_{nk}} \right)^{x_n} \left( \prod_k X_k^{B_{nk}} Z_k^{C_{nk}} \right)^{z_n} \end{aligned} \quad (\text{B2})$$

Our goal is to rearrange the above expression as  $P' = i^s \prod_k X_k^{x'_k} Z_k^{z'_k}$ . To this end, we need to commute the  $X$  operators through the  $Z$  operators such that the  $X/Z$ 's acting on the same site can be combined together. This process will give an extra sign factor as  $(-1)^{s'}$  with

$$\begin{aligned} s' &= \sum_{n=1}^N \sum_{k=2}^N \left( \sum_{k'=1}^{k-1} F_{nk'} x_n + C_{nk'} z_n \right) (B_{nk} z_n + D_{nk} x_n) \\ &\quad + \sum_{n=1}^N \sum_{k=1}^N F_{nk} x_n B_{nk} z_n \end{aligned} \quad (\text{B3})$$

It is easy to verify that this extra sign factor is taken into account by Line 16 in Algorithm 4.

While a stabilizer tableau can be efficiently constructed when appending simple Clifford gates (e.g., CNOT, H, or S gates) to a larger Clifford circuit with a known stabilizer tableau [8, 9, 23], here we provide the formal update method for stabilizer tableau when two arbitrary Clifford circuits are concatenated. This is summarized in the following proposition:

**Proposition 1** (*Concatenation of Clifford circuits*) Let  $U_1$  and  $U_2$  be two  $N$ -qubit Clifford circuits with stabilizer tableaux  $\{\mathbf{g}^{[1]}, \mathbf{a}^{[1]}, \mathbf{D}^{[1]}, \mathbf{F}^{[1]}, \mathbf{B}^{[1]}, \mathbf{C}^{[1]}\}$  and  $\{\mathbf{g}^{[2]}, \mathbf{a}^{[2]}, \mathbf{D}^{[2]}, \mathbf{F}^{[2]}, \mathbf{B}^{[2]}, \mathbf{C}^{[2]}\}$ , respectively. Then, the stabilizer tableau for the concatenated circuit  $U_C = U_2 U_1$  is given by  $\{\mathbf{g}, \mathbf{a}, \mathbf{D}, \mathbf{F}, \mathbf{B}, \mathbf{C}\}$ , as follows:

$$\mathbf{D} = \mathbf{D}^{[2]} \mathbf{D}^{[1]} + \mathbf{F}^{[2]} \mathbf{B}^{[1]}, \quad \mathbf{F} = \mathbf{D}^{[2]} \mathbf{F}^{[1]} + \mathbf{F}^{[2]} \mathbf{C}^{[1]}, \quad (\text{B4})$$

$$\mathbf{B} = \mathbf{B}^{[2]} \mathbf{D}^{[1]} + \mathbf{C}^{[2]} \mathbf{B}^{[1]}, \quad \mathbf{C} = \mathbf{B}^{[2]} \mathbf{F}^{[1]} + \mathbf{C}^{[2]} \mathbf{C}^{[1]}, \quad (\text{B5})$$

$$\begin{aligned} g_n &= g_n^{[2]} + \sum_{k=1}^N (D_{nk}^{[2]} g_k^{[1]} + F_{nk}^{[2]} a_k^{[1]}) + 2 \sum_{k,l=1}^N D_{nk}^{[2]} F_{nk}^{[2]} F_{kl}^{[1]} B_{kl}^{[1]} \\ &\quad + \sum_{l=1}^N \sum_{k=2}^N \sum_{k'=1}^{k-1} (D_{nk'}^{[2]} F_{k'l}^{[1]} + F_{nk'}^{[2]} C_{k'l}^{[1]}) (D_{nk}^{[2]} D_{kl}^{[1]} + F_{nk}^{[2]} B_{kl}^{[1]}), \end{aligned} \quad (\text{B6})$$

$$\begin{aligned} a_n &= a_n^{[2]} + \sum_{k=1}^N (B_{nk}^{[2]} g_k^{[1]} + C_{nk}^{[2]} a_k^{[1]}) + 2 \sum_{k,l=1}^N B_{nk}^{[2]} C_{nk}^{[2]} F_{kl}^{[1]} B_{kl}^{[1]} \\ &\quad + \sum_{l=1}^N \sum_{k=2}^N \sum_{k'=1}^{k-1} (B_{nk'}^{[2]} F_{k'l}^{[1]} + C_{nk'}^{[2]} C_{k'l}^{[1]}) (B_{nk}^{[2]} D_{kl}^{[1]} + C_{nk}^{[2]} B_{kl}^{[1]}). \end{aligned} \quad (\text{B7})$$

Eq. (B4) and (B5) involve straightforward matrix multiplications and are thus computationally manageable. While the phase factor calculations Eq. (B6) and (B7) may appear more intricate, they can be implemented efficiently by counting how many times Pauli  $X$  operators with the Pauli  $Z$  operators and consolidating the Pauli  $X/Z$  for each qubit. This approach requires only tracking the number of anti-commuting  $Z$  operators preceding each Pauli  $X$  operator, a strategy that applies identically in Algorithm 4.

Here we prove Proposition 1 by deriving Eq. (B4) and (B6), whereas the other two formulas can be derived similarly.

$$\begin{aligned} U_C^\dagger X_n U_C &= U_1^\dagger (U_2^\dagger X_n U_2) U_1 \\ &= i^{g_n^{[2]}} \prod_{k=1}^N (U_1^\dagger X_k U_1)^{D_{nk}^{[2]}} (U_1^\dagger Z_k U_1)^{F_{nk}^{[2]}} \\ &= i^{g_n^{[2]}} \prod_{k=1}^N \left( i^{g_k^{[1]}} \prod_{l=1}^N X_l^{D_{kl}^{[1]}} Z_l^{F_{kl}^{[1]}} \right)^{D_{nk}^{[2]}} \left( i^{a_k^{[1]}} \prod_{l=1}^N X_l^{B_{kl}^{[1]}} Z_l^{C_{kl}^{[1]}} \right)^{F_{nk}^{[2]}} \end{aligned} \quad (\text{B8})$$

From the above expression, it is easy to see that

$$D_{nl} = \sum_{k=1}^N D_{nk}^{[2]} D_{kl}^{[1]} + F_{nk}^{[2]} B_{kl}^{[1]} \quad (\text{B9})$$

$$F_{nl} = \sum_{k=1}^N D_{nk}^{[2]} F_{kl}^{[1]} + F_{nk}^{[2]} C_{kl}^{[1]} \quad (\text{B10})$$

which are exactly the results from Eq. (B4). As of the exponent for the phase factor, i.e.,  $g_n$ , we do the same procedure as for Algorithm 4, that is, recording the additional sign factors from the process of commuting the  $X$  operators through the  $Z$  operators. This process eventually produces Eq. (B6). For algorithm implementation, the phase factor can be computed in a similar way to Algorithm. 4.

### Appendix C: Derivation for Eq. (18)

Here we provide the derivation for Eq. (18). First, we rewrite Eq. (17) as

$$t_{\text{free}} = N + \sum_{N_m=1}^N \frac{1}{2^{N_m-1}}. \quad (\text{C1})$$

On the one hand, we have

$$\frac{1}{2^{N_m-1}} > \frac{1}{2^{N_m}} \quad (\text{C2})$$

which gives

$$t_{\text{free}} > N + \sum_{N_m=1}^N \frac{1}{2^{N_m}} = N + 1 - \frac{1}{2^N} \quad (\text{C3})$$

On the other hand, we have

$$\frac{1}{2^{N_m-1}} = \frac{\frac{1}{2^{N_m}}}{1 - \frac{1}{2^{N_m}}} < \frac{2}{2^{N_m}} \quad (\text{C4})$$

which gives

$$t_{\text{free}} < N + \sum_{N_m=1}^N \frac{2}{2^{N_m}} = N + 2 - \frac{1}{2^{N-1}}. \quad (\text{C5})$$

### Appendix D: Improved Stabilizer Group Learning Algorithm

In this section we present an improved algorithm to compute the stabilizer nullity efficiently, one of the measures for quantum magic. Nullity has been studied as a crucial quantity for the boundary of classical simulability [40], and here will provide further insights on the classical simulation of  $t$ -doped Clifford circuits with Clifford-MPS states. Stabilizer nullity is defined as  $\nu = N - |G|$ , where  $G$  is a generator set (of size  $|G|$ ) that produces Pauli strings  $\sigma$  (stabilizers) satisfying  $|\langle \psi | \sigma | \psi \rangle| = 1$ .

To compute the stabilizer nullity, or equivalently, determine the number of stabilizer generators  $|G|$  for Clifford-MPS states, we employ an algorithm improved upon the one from Ref. [44]. And as we will show soon, the improvement reduces the original exponential cost to a linear cost. The algorithm leverages a theorem (for convenience, we call it as *threshold condition* here) from Ref. [44]:

**Theorem 1** (*Threshold condition Ref. [44]*) *Given an  $N$ -qubit matrix product state  $|\psi\rangle = \sum_{\mathbf{s}} \mathbb{A}_1^{s_1} \mathbb{A}_2^{s_2} \cdots \mathbb{A}_N^{s_N} |\mathbf{s}\rangle$ , where  $\mathbf{s} = (s_1, s_2, \dots, s_N)$ , and  $\mathbb{A}_j^{s_j}$  are  $\chi_{j-1} \times \chi_j$  matrices ( $\chi_0 = \chi_N = 1$ ), if an  $N$ -qubit Pauli string  $\sigma \equiv \sigma_1 \sigma_2 \cdots \sigma_N$  stabilizes  $|\psi\rangle$ , i.e.,  $\sigma |\psi\rangle = \pm |\psi\rangle$ , then the marginal probability of any first  $n$ -qubit substring  $\sigma_{1:n} \equiv \sigma_1 \sigma_2 \cdots \sigma_n$  from  $\sigma$ , which is defined by  $\pi(\sigma_{1:n}) = \sum_{\sigma'_{n+1:N}} \Pi(\sigma_{1:n} \sigma'_{n+1:N})$  and  $\Pi(\sigma_{1:n} \sigma'_{n+1:N}) = \frac{1}{2^N} |\langle \psi | \sigma_{1:n} \sigma'_{n+1:N} | \psi \rangle|^2$ , must satisfy*

$$\pi(\sigma_{1:n}) \geq \frac{1}{2^n \chi_n} \quad (\text{D1})$$

*For right-normalized  $|\psi\rangle$ , i.e.,  $\sum_{s_j} \mathbb{A}_j^{s_j} (\mathbb{A}_j^{s_j})^\dagger = \mathbb{1}$ ,  $\pi(\sigma_{1:n})$  can be efficiently calculated as*

$$\begin{aligned} \pi(\sigma_{1:n}) &= \text{Tr}(\mathbb{L}(\sigma_{1:n})^\dagger \mathbb{L}(\sigma_{1:n})), \text{ with} \\ \mathbb{L}(\sigma_{1:n}) &= \frac{1}{\sqrt{2}} \sum_{s', s} \sigma_n^{s' s} (\mathbb{A}_n^{s'})^\dagger \mathbb{L}(\sigma_{1:n-1}) \mathbb{A}_n^s, \quad (\text{D2}) \\ \mathbb{L}(\sigma_{1:0}) &= \mathbb{1}. \end{aligned}$$

The original algorithm's primary insight is that only Pauli strings meeting the threshold condition during autoregressive sampling from qubit 1 to  $N$  are retained. Our improvement reduces redundancy by tracking only

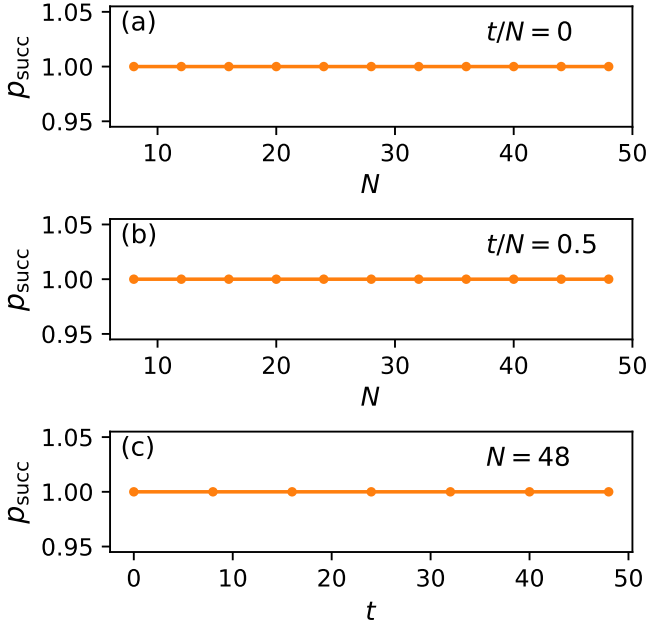


FIG. 20: Success probabilities of the stabilizer group learning algorithm finding the correct stabilizer group for  $U_C|N, t\rangle$  with (a)  $t/N = 0$ , (b)  $t/N = 0.5$  and (c)  $N = 48$ . Each data point averages over 1,000 random realizations of  $U_C|N, t\rangle$ .

the maximal generator set (via methods like Gaussian elimination) for Pauli substrings that satisfy the threshold condition throughout the autoregressive sampling. The complete algorithm is detailed in Algorithm 5.

---

**Algorithm 5** Stabilizer group learning algorithm for MPS

---

**Input:** an  $N$ -qubit right-normalized MPS  $|\psi\rangle$ .

- 1: Initialize: Generator set  $G = \{\}$ .
- 2: **for**  $n = 1, 2, \dots, N$  **do**
- 3:   Initialize: Pauli substring set  $\Sigma = \{\}$ .
- 4:   Compute  $\pi(\sigma_{1:n-1}\sigma_n)$  for  $\sigma_n \in \{I, X, Y, Z\}$  and  $\sigma_{1:n-1} \in G$ .
- 5:   Add  $\sigma_{1:n-1}\sigma_n$  to  $\Sigma$  **if**  $\pi(\sigma_{1:n-1}\sigma_n) \geq 1/(2^n \chi_n)$ .
- 6:   Sort  $\Sigma$  in descending order according to  $\pi(\sigma_{1:n})$ .
- 7:    $G = \{\}$ .
- 8:   **for** ( $j = 1, 2, \dots, |\Sigma|$ ) **do**
- 9:     Add  $\sigma^j$  to  $G$  **if**  $\sigma^j \in \Sigma$  cannot be generated by  $G$ .
- 10:   **end for**
- 11: **end for**

**Output:** stabilizer group generators  $G = \{\sigma^j\}_{j=1}^{|G|}$  for  $|\psi\rangle$ .

---

As a benchmark, we test this algorithm on MPS for states prepared as  $U_C|N, t\rangle$ , where  $U_C$  is an 1D brick-wall circuit with random 2-qubit Clifford gates, and  $|N, t\rangle =$

$|+\rangle^{\otimes N-t}|m\rangle^{\otimes t}$ , with  $|+\rangle = (|0\rangle + |1\rangle)/\sqrt{2}$  and  $|m\rangle$  being random single-qubit non-stabilizer states. Fig. 20 shows 100% success rate over 1,000 random realizations of  $U_C|N, t\rangle$  for various values of  $N$  and  $t$ .

In fact, the Clifford disentangling algorithm from Sec. IIB is also applicable to the learning of stabilizer group for MPS as well as the calculation of stabilizer nullity. However, since it is a heuristic optimization algorithm, it might suffer from the issues of local minima or barren plateaus. The improved algorithm in this section is deterministic and more efficient for stabilizer group learning.

As have been noted, the purpose of reserving only the generator set, rather than all the Pauli strings as done in the original algorithm, is to reduce redundancy. The generator set is sufficient to describe the entire stabilizer group, which contains an exponential number of elements. Specifically, suppose  $\{\sigma^1, \sigma^2, \dots, \sigma^{|G|}\}$  are the stabilizer generators for the MPS  $|\psi\rangle$ . Their substrings, up to the  $n$ -th qubit,  $\{\sigma_{1:n}^1, \sigma_{1:n}^2, \dots, \sigma_{1:n}^{|G|}\}$ , will be included in the Pauli string set that satisfies the threshold condition up to the  $n$ -th qubit. The group generated from them, which is of size at most  $2^{|G|}$ , will also be included. Since these Pauli strings will always satisfy the threshold condition in the remaining sampling steps, we can avoid this exponential overhead by keeping track of the generator set until the end. However, it might occur that two Pauli substrings  $\tilde{\sigma}_{1:n}^1, \tilde{\sigma}_{1:n}^2$ , which individually are not stabilizer Pauli substrings, can combine to form a stabilizer Pauli substring  $\sigma_{1:n} = \tilde{\sigma}_{1:n}^1 \tilde{\sigma}_{1:n}^2$ , and get selected into the reserved generator set, i.e.,  $\{\tilde{\sigma}_{1:n}^1, \tilde{\sigma}_{1:n}^2, \dots, \sigma_{1:n}^{|G|}\}$ . This would result in a final generator set that misses two correct stabilizer generators. Fortunately, based on the benchmarking results (Fig. 20), the improved algorithm seems to be able to rule out this possibility.

As a result, the stabilizer group learning algorithm for MPS is improved in the following aspects: (1) Only a single iteration over the qubits is required to learn all the stabilizer generators. (2) No additional Clifford circuit layers are needed to modify the MPS for sampling the undiscovered stabilizers as done in the original algorithm. (3) Since the maximum number of generators for the  $n$ -qubit Pauli substrings is  $2n$ , the maximal number of reserved Pauli substrings during the autoregressive sampling do not need to be a heuristically tuned parameter for large system sizes and now is determinable as  $2N$ .

### Appendix E: Alternative View on the $t$ -doped Clifford Circuits Simulation

In this section, we provide an alternative view on the classical simulation of  $t$ -doped Clifford circuits with CAMPS. We start with the empirical observations before putting forward the criterion for the classical simulability based on the principle of OFD.

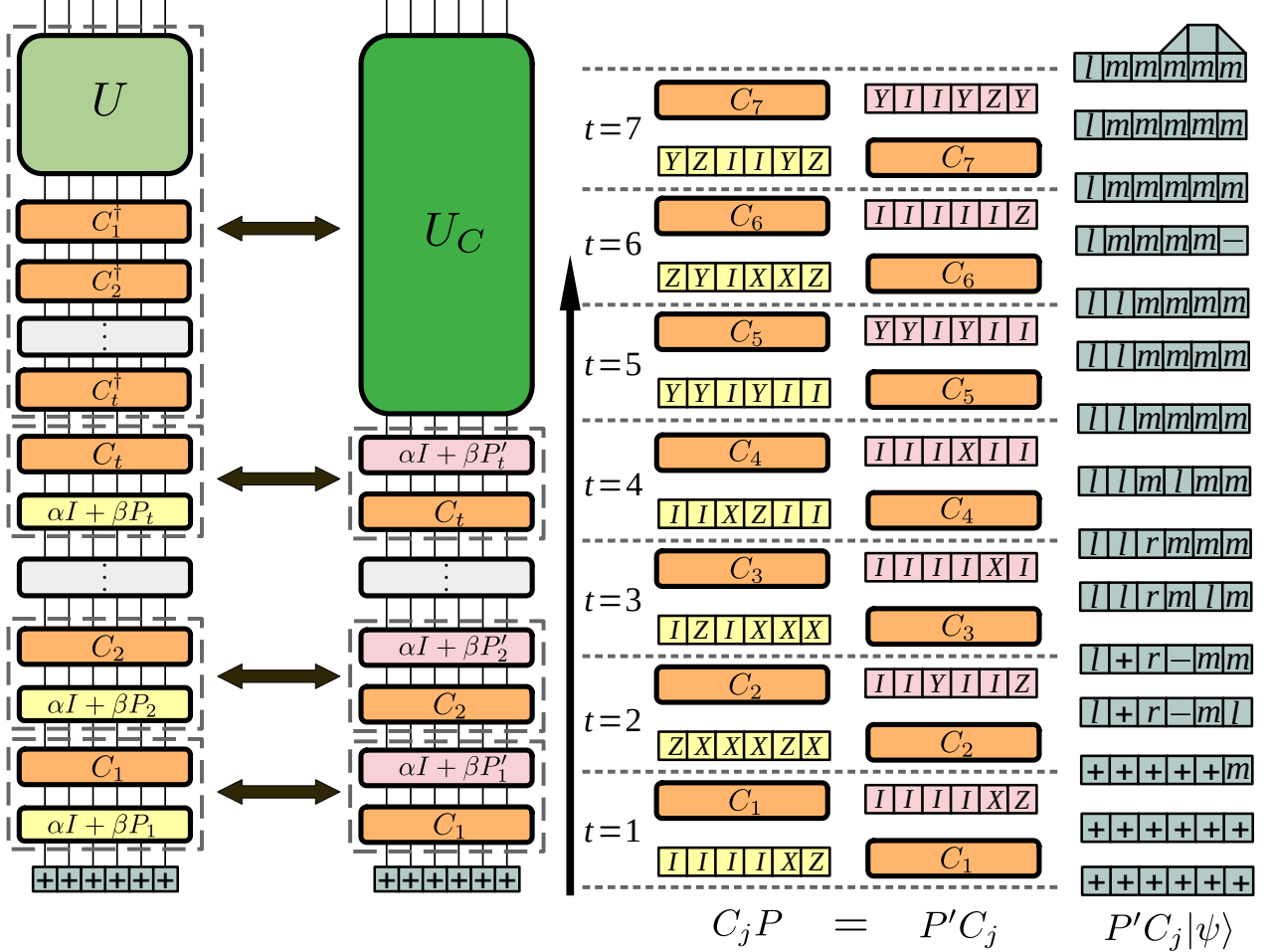


FIG. 21: Visualization of the simulation of  $t$ -doped Clifford circuits with CAMPS.

In Fig. 21, we present a schematic diagram illustrating the evolution of CAMPS for a real circuit example ( $N = 6$ ,  $N_T = 1$ ). Initially,  $T$ -gates are injected into the Clifford circuit  $U$ . During the simulation, the Clifford gates are absorbed into the stabilizer tableau, while the non-Clifford  $T$ -gates are commuted through the Clifford gates, resulting in twisted operators adjacent to  $|\psi\rangle$ . Specifically, as shown on the left of Fig. 21, each block labeled  $\alpha I + \beta P_j$  ( $j = 1, 2, \dots, t$ ) represents the twisted operator from the  $j$ -th  $T$ -gate:

$$T^{[j]} U \prod_{k=1}^{j-1} C_k^\dagger = U \left( \prod_{k=1}^{j-1} C_k^\dagger \right) (\alpha I + \beta P_j) \quad (\text{E1})$$

where  $C_k$  is the disentangling Clifford circuit from the Clifford disentangling algorithm for  $k$ -th  $T$ -gate.  $C_j$  is inserted into the circuit as  $C_j^\dagger C_j$ , and  $C_j^\dagger$  is absorbed into the stabilizer tableau for the Clifford circuit, denoted as  $U_C$  in Fig. 21, while  $C_j$  and  $\alpha I + \beta P_j$  are absorbed into  $|\psi\rangle$  together to reduce its entanglement.

Now, alternatively, after identifying  $C_j$ , instead of al-

lowing the twisted operator  $\alpha I + \beta P_j$  to act on the MPS  $|\psi\rangle$  first, we can commute it backwards. Specifically, we apply Algorithm 4 to find  $P'_j = C_j P_j C_j^\dagger$  such that  $C_j (\alpha I + \beta P_j) |\psi\rangle = (\alpha I + \beta P'_j) C_j |\psi\rangle$ , as illustrated from the left half side of Fig. 21. By doing so,  $C_j$  acts on  $|\psi\rangle$  first, and we then examine how the new twisted operator  $\alpha I + \beta P'_j$  modifies the resulting  $C_j |\psi\rangle$ .

On the right side of Fig. 21, we provide an visualization of this simulation process. The yellow blocks in the left column represent  $P_j$ , the pink blocks in the middle column correspond to  $P'_j$ , and the blue blocks in the right column show the states  $|\psi\rangle$  after the actions of the operators beneath them. For instance, the third blue block from the bottom,  $|++++m\rangle$  is equivalent to  $(\alpha I + \beta IIIIXZ)C_1|++++\rangle$ , and the fourth block,  $|l+r-ml\rangle$ , corresponds to  $C_2|++++m\rangle$ . Here the eigenstates for the Pauli operators  $\{X, Y, Z\}$  with eigenvalues  $\pm 1$  are denoted as  $+/-$ ,  $l/r$  and  $0/1$ , respectively, while the magic states are represented as  $m$ . The height of the blocks reflects the bond dimension within the MPS. For example, the last blue block has its fifth component

with height 2 on both sides, indicating the matrix for the fifth qubit is  $2 \times 2$ , meaning this qubit is entangled with its two neighbors. In contrast, all other blocks have a height of 1 for each component, indicating that they are product states.

Based on the visualization of the simulation process, we heuristically conclude that two conditions must be met simultaneously to prevent an increase in entanglement within the MPS:

- (C1): When the disentangling Clifford circuit  $C_j$  for the  $j$ -th  $T$ -gate transforms the MPS  $|\psi_j\rangle$  into  $|\psi'_j\rangle = C_j|\psi_j\rangle$ , it preserves the bond dimension of the MPS. In other words, if  $|\psi_j\rangle$  is a product state,  $|\psi'_j\rangle$  remains a product state;
- (C2): The Pauli string  $P'_j$  may contain multiple non-identity operators, but its effect on  $|\psi'_j\rangle$  must be equivalently to that of another Pauli string  $\tilde{P}'_j$ , which has only one non-identity operator acting on  $|\psi'_j\rangle$ , i.e.,  $\tilde{P}'_j|\psi'_j\rangle = P'_j|\psi'_j\rangle$ . If the qubit affected by the non-identity operator is an eigenstate of a Pauli operator, it becomes a magic qubit after the action of  $\alpha I + \beta P'_j$ ; if it is already a magic qubit, the entanglement of the MPS remains unchanged, and the number of magic qubits does not increase.

These conditions (C1) and (C2) can be verified from the example in Fig. 21. Notably, whenever either of these conditions is violated, entanglement increases. For instance, at the final step ( $t = 7$ ) in Fig. 21, the effect of  $P'_7$  cannot be reduced to a Pauli string with only one non-identity Pauli operator, causing the fifth qubit to become entangled with its neighbors.

### Appendix F: Conjectures for an Ideal Clifford disentangling Algorithm

Throughout this work, we introduced two Clifford disentangling algorithms for simulating  $t$ -doped Clifford circuits: the first algorithm finds an optimal two-qubit Clifford gate to minimize entanglement (Sec. II B), while the second utilizes control gates to reduce discrepancies (i.e., the number of qubits in differing states) between the combined quantum states (Sec. II A). Both methods belong to *local* Clifford disentangling algorithms, leveraging only local quantum information and two-qubit Clifford operations. We have also identified cases where these local techniques fail to reduce MPS entanglement. However, it remains as an open question whether we can find a *global* Clifford disentangling algorithm that utilizes the global information of states and the full  $N$ -qubit Clifford group.

In this section, instead of developing a global algorithm, we propose conjectures about its potential properties, should such a method be devised for simulating  $t$ -doped Clifford circuits.

We formalize the simulation process slightly different from the main text, though effectively they are equivalent. For a given  $t$ -doped Clifford circuit, we first commute all  $T$ -gates toward the MPS, which is in the state  $|00\dots 0\rangle$  initially. This yields a set of Pauli strings  $P_{j=1}^t$ , allowing us to represent the state to be simulated as

$$|\Psi\rangle = U \prod_{j=1}^t (\alpha I + \beta P_j) |00\dots 0\rangle \quad (\text{F1})$$

For a global Clifford disentangling algorithm, we anticipate finding an  $N$ -qubit Clifford circuit  $C$  that retains the MPS as a product state. Specifically, we would have:

$$\begin{aligned} |\Psi\rangle &= U \prod_{j=1}^t (\alpha I + \beta P_j) C^\dagger C |00\dots 0\rangle \\ &= UC^\dagger \prod_{j=1}^t (\alpha I + \beta P'_j) C |00\dots 0\rangle \end{aligned} \quad (\text{F2})$$

where  $P'_j = CP_jC^\dagger$ . The first desirable property for such an algorithm is:

- (P1):  $C|00\dots 0\rangle$  is a product state.

Thus, we can write as  $C|00\dots 0\rangle = \otimes_{k=1}^N |s_k\rangle$ , where  $|s_k\rangle$  is an eigenstate of Pauli operator. Furthermore, as we will show later, we can transform  $|s_k\rangle$  back to  $|0\rangle$  without altering the results.

The second desired property concerns the commutation structure of the transformed set  $\{P'_j\}$ , which retains the commutation relations of  $\{P_j\}$ . We define a commutation table  $\mathbb{S}$ , where each element  $\mathbb{S}_{jk} \in \{0, 1\}$  encodes the commutation relation between  $P_j$  and  $P_k$ :  $P_j P_k = (-1)^{\mathbb{S}_{jk}} P_k P_j$ . Consequently,  $\mathbb{S}$  is Hermitian and  $\mathbb{S}_{jj} = 0$ . Additionally, we define a table  $\mathbb{P}$  for the transformed operators  $\{P'_j\}$ , with entries  $\mathbb{P}_{jk}$  denoting the Pauli operator of  $P'_j$  on the  $k$ -th qubit. To ensure that  $|\Psi\rangle$  retains a product state structure in the MPS portion, we conjecture the second property as:

- (P2): Given  $C|00\dots 0\rangle = |00\dots 0\rangle$ ,  $C$  transforms  $\{P_j\}$  to  $\{P'_j\}$  so that  $\mathbb{P}_{jj} = Z$  and  $\mathbb{P}_{jk} = X^{\mathbb{S}_{jk}}$  for  $j \neq k$ .

This construction preserves the commutation relations of  $\{P_j\}$ . For instance, at  $N = 4$ ,  $t = 3$ , given

$$\mathbb{S} = \begin{bmatrix} 0 & 0 & 1 \\ 0 & 0 & 1 \\ 1 & 1 & 0 \end{bmatrix}, \quad (\text{F3})$$

according to (P2), we obtain

$$\mathbb{P} = \begin{bmatrix} Z & I & X & I \\ I & Z & X & I \\ I & I & Z & I \end{bmatrix} \quad (\text{F4})$$

This setup allows the operators  $\prod_{j=1}^t (\alpha I + \beta P'_j)$  acting on  $C|00\dots 0\rangle = |00\dots 0\rangle$  to produce at most one magic

qubit. The example above, for instance, yields  $|00m0\rangle$ . However, this construction ceases to work if  $t > N$ , at which point the MPS begins to develop entanglement.

Lastly, we present an alternative form of (P2) for cases where  $C$  maps  $|0\rangle$  to another eigenstate ( $|s_k\rangle$ ) of Pauli operator  $P[s_k]$ :

(P2'): Given  $C|00\dots 0\rangle = \otimes_{k=1}^N |s_k\rangle$ ,  $C$  transforms  $\{P_j\}$  to  $\{P'_j\}$ , so that  $\mathbb{P}_{jj} = P[s_j]$  and  $\mathbb{P}_{jk} = \bar{P}[s_k]^{\mathbb{S}_{jk}}$ ,  $j \neq k$ .

where  $\bar{P}[s_k]$  is a Pauli operator other than  $P[s_k]$ . The two properties (P2) and (P2') are equivalent. This equivalence is confirmed by noting the existence of a single-qubit Clifford gate  $U(s_k)$  that transforms  $|s_k\rangle$  back to  $|0\rangle$ , i.e.,  $U(s_k)|s_k\rangle = |0\rangle$ . Meanwhile,  $U(s_k)P[s_k]U(s_k)^\dagger = Z$ , and  $U(s_k)P[s_k]U(s_k)^\dagger = \bar{Z}$ , where  $\bar{Z}$  is a Pauli operator other than  $Z$ . Therefore, if we let

$$C \leftarrow \left( \prod_{k=1}^N U(s_k) \right) C|00\dots 0\rangle \quad (\text{F5})$$

we will get

$$P'_j \leftarrow \left( \prod_{k=1}^N U(s_k) \right) P_j \left( \prod_{k=1}^N U(s_k) \right)^\dagger \quad (\text{F6})$$

which is exactly the construction from (P2).

## Appendix G: Numerical Results on Pauli Observeables

Besides the observables from the main text, we also compare the observable expectation from Clifford-MPS with those from MPS. In Fig. 22, we show  $\varepsilon_{\max}$  versus MPS bond dimension  $\chi_{\max}$  and  $T$  gate number  $t$ .  $\varepsilon_{\max}$  is evaluated as follows: we use the exact wave function (MPS with full bond dimension  $\chi_{\max} = 2^{N/2}$ ) to sample a set of Pauli strings  $\{P_j\}_{j=1}^J$  and the corresponding exact expectations  $\{p_j\}_{j=1}^J$  (total number  $J = 1000$  here); next we use Clifford-MPS and MPS with varying  $\chi_{\max}$  to evaluate the expectation  $\{p_j^c\}_{j=1}^J$ ,  $c \in \{\text{CAMPS}, \text{MPS}\}$  respectively; at last, we use

$$\varepsilon_{\max}^c = \max_j |p_j^c - p_j| \quad (\text{G1})$$

to evaluate the accuracy of Clifford-MPS or MPS. Note that when circuits get deeper, the density matrix of the states will distribute the weights over more Pauli strings, and have smaller expectation values for Pauli strings, thus we observe smaller absolute errors at large  $t$  from Fig. 22. The later rise of errors from CAMPS suggests more accurate representation ability from CAMPS than MPS.

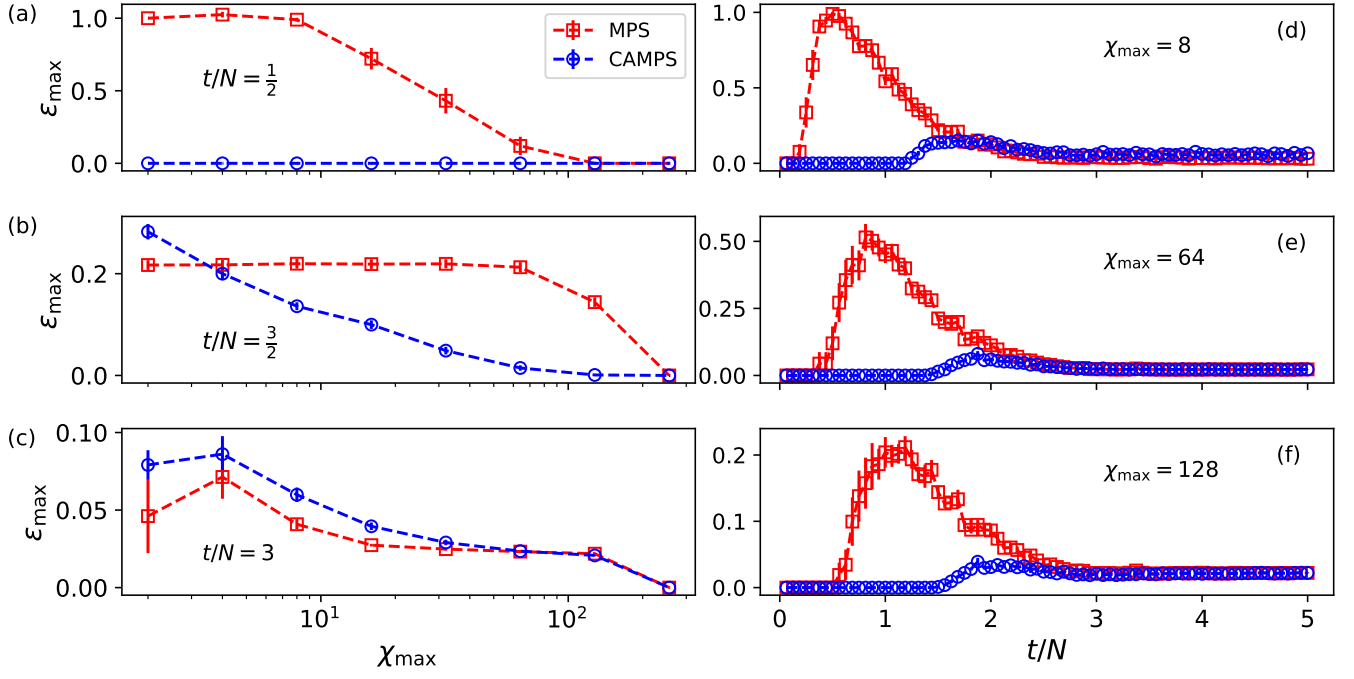


FIG. 22: Maximum error  $\epsilon_{\max}$  of the expectation from the sampled Pauli string set ( $N = 16$ ,  $N_T = 1$ ) with varying maximal MPS bond dimension  $\chi_{\max}$ . Each data is averaged over 16 circuit realizations and error bars are present.